Enhanced control of the turbulent flow past a circular cylinder with rotating rods inspired by an inviscid solution

I. A. Carvalho[a,*], G. R. S. Assi[b]

[a] *Department of Mechanical Engineering, EPUSP, University of São Paulo, Brazil*
[b] *Department of Naval Architecture & Ocean Engineering, EPUSP, University of São Paulo, Brazil*

Abstract

This paper examines an active mechanism of wake control for a turbulent flow regime of Reynolds number 1000 through finite volume, three-dimensional DES simulations. Eight peripheral rods equally spaced about a central body are forced to spin around their axes in two arrangements: case 0, with uniform rotation speed and case 1, with rotation rates inspired by the solution of the potential flow around the body. The two cases were constrained to the same input kinetic energy for every set of rotations. We have found case 1 to be more effective to control the wake, eliminate turbulent structures, and attenuate mean drag and fluctuating lift. The interference of the rods in the flow past the main body resulted in a steady wake in both cases, provided enough rotation was supplied to the system. This result was previously achieved only in laminar regime. Novel to such a system, rotations midway between a vortex wake and a steady wake led streamwise vortices to show a mode-B-like mechanism of vorticity transfer. Case 1 generally suppressed vortex shedding with lower input kinetic energy and required less power than case 0, thus resulting in a more efficient configuration to suppress vortices in the wake.

Keywords: Vortex-shedding suppression, wake control, drag reduction, bluff body.

1. Introduction

Oil and gas exploration in ultra-deep waters has motivated the design of large offshore marine structures of circular cross-section, such as monocolumns and spar platforms (Gonçalves et al., 2011), that allow for the exploration of reservoirs in ultra-deep waters. These platforms are subjected to the effect of sea currents, whereby the interaction with the bluff structure leads to alternate vortex shedding in the wake past the body, generating the so-called *Kármán vortex street*.

*Corresponding author: amorim.icaro@usp.br (I. A. Carvalho)

Published article (in its final form: July, 2022):
Carvalho, I. A., and G. R. S. Assi. "**Enhanced control of the turbulent flow past a circular cylinder with rotating rods inspired by an inviscid solution**" Journal of Fluids and Structures 113 (2022):103652. **https://doi.org/10.1016/j.jfluidstructs.2022.103652**

The cyclic loads produced by the phenomenon of *vortex shedding* may cause the structure to respond with *vortex-induced vibrations* (VIV), a periodic motion both streamwise and in the transverse direction, caused by the components of the resultant force, respectively denoted drag and lift. As the vortex-shedding frequency nears and locks onto the natural frequency of the body, progressively larger amplitudes of motion develop. Fatigue and failure of slender structures have been reported as some of the adverse outcomes of VIV. This rather minute overview of VIV can be expanded by the comprehensive review of Williamson and Govardhan (2004) and the references therein. Considering the response of large floating structures, the same physical mechanism has been termed *vortex-induced motion* (VIM) due to its low-frequency characteristics (Fujarra et al., 2012; Gonçalves et al., 2011).

Techniques to suppress vortex-shedding, reduce oscillating loads and avoid VIV have been fostered by a wealth of studies. The seminal paper of Strykowski and Sreenivasan (1990) elucidated, through experiments and numerical simulations, that the proper placement of a single control cylinder (a smaller rod near the main, larger body) could suppress entirely the instabilities that otherwise led to vortex shedding at low Reynolds numbers (Re). Later, Mittal and Raghuvanshi (2001) conducted numerical investigations and found that this passive mechanism reduced the mean drag even in the turbulent regime of $Re = 10,000$, although it could not prevent vortex shedding or the formation of three-dimensional structures in the wake.

More recently, experiments performed by Cicolin et al. (2021) with one rod at different locations around a central cylinder employing particle-image velocimetry at $Re = 20,000$ advanced on two matters: i) on the details of the interaction between the control rod and the shear layer of the main body and ii) on the influence of the control rod on separation. The authors remarked on a significant influence of the position of the separation point on drag and lift measurements in turbulent regime. Interestingly, the insertion of the control rod within the recirculation zone had little effect upon the drag of the main body.

Complex systems involving multiple rods can be engineered to achieve greater flow control. Axisymmetric arrangements with 2, 4 and 8 rods around the main cylinder, as in figure 1, were tested by Silva-Ortega and Assi (2017b) varying rod diameter and gap at Re between 5×10^3 and 5×10^4. The authors revealed that a galloping-like response was produced using 4 rods, and a decrease in drag was obtained. For 8 rotating rods, an omnidirectional-like system strongly

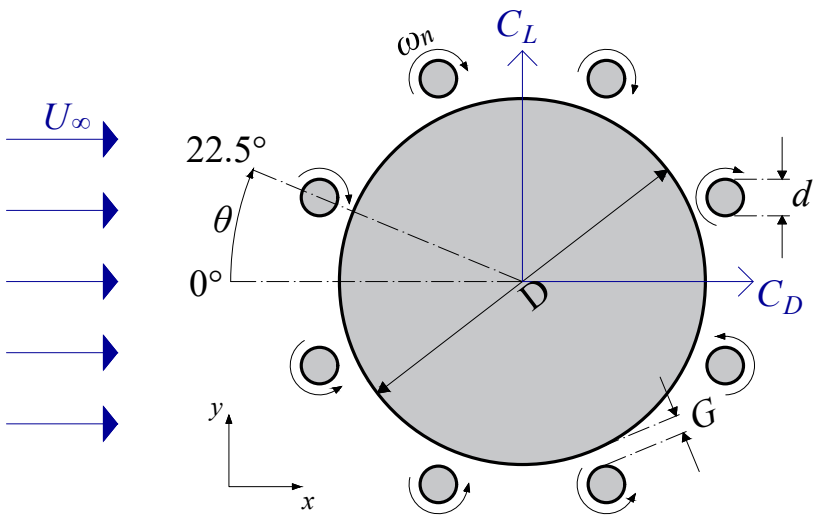

Figure 1: Uniform flow past a system comprised by a main cylinder and rotating control rods.

reduced VIV, also generating negative drag for higher rotation speeds. Under any configuration, it was reported that, in general, the presence of the rods around the main cylinder reduced the response amplitude. Building on the vortex-shedding mechanism proposed by Gerrard (1966) one can infer that this interference with control rods might be disrupting the communication between the shear layers. Through sensitivity analysis, Patino et al. (2017) referred to the stabilising effect of the (passive and active) rods as a consequence of the cutback in circulation being supplied to the near-wake region.

The passive mechanism in conjunction with power input to spin the rods, and thus to impart momentum into the shear layers, gave rise to the active mechanism of Moving Surface Boundary-layer Control (MSBC). Active and passive control techniques were thoroughly reviewed by Zdravkovich (1981) and Choi et al. (2008). We simply surmise that MSBC has been proven effective to mitigate drag in bluff bodies (Modi et al., 1990) and to reduce the total variance in the cylinder wake, as well as to render the streamwise velocity profile more uniform (Korkischko and Meneghini, 2012). Some of the previous works in this matter employed a system such as that of Silva-Ortega and Assi (2017b) with 8 rods.

In laminar regime, Assi et al. (2019) demonstrated through two-dimensional, finite volume simulations at $Re = 100$ that the setup of eight control rods spinning at a uniform speed (equal to three times that of the free stream) could suppress vortex shedding. Sufficient spinning beyond this critical value gave rise to thrust (negative drag) on the entire system. With a similar setup,

however, in turbulent flow regime, the MSBC technique allowed Assi et al. (2018) to extend the interval of Reynolds numbers where reduction in the fluctuating loads was obtained up to $Re = 10,000$, even though full vortex-shedding suppression was not achieved. Silva-Ortega and Assi (2017b) investigated the active interference of the rods with crosswise VIV and reported lowered hydrodynamic loads and peak amplitude in the oscillatory motion for the same setup of 8 rods and Re range as Silva-Ortega and Assi (2017b), but suppression was not achieved either.

In line with these previous works, Carvalho et al. (2021) approached the same problem in a laminar regime with a methodology inspired by potential-flow theory that defined the rotation rates of the rods (to be explained in detail in section 2). Surely, different rods relative to the main body and to the separation of the flow differed in relevance with respect to one another. Comparing the work of Carvalho et al. (2021) with that of Assi et al. (2019), the new setup – with the same input kinetic energy – seemed to present lower drag obtained by a slightly greater power requirement.

It seems, to the best our knowledge, that there is still room for the investigation of a setup such as that of Silva-Ortega and Assi (2017b) (with 8 rods) in regards to complete suppression of vortex shedding in turbulent regime and to considerations of streamwise vorticity, which are lacking in previous analyses. We now follow this thread and retain the potential-flow-inspired angular speeds, but for a turbulent regime (as opposed to laminar regime in Carvalho et al. (2021)) and seek to evaluate how the system of figure 1 responds in turbulent flows.

1.1. Objective

The present paper focuses on the flow response to a progressive increase in the angular velocities of the eight control rods placed around the main body, as shown in figure 1. Our motivation is to explore this active mechanism for wake control and suppression of vortex shedding. More specifically, we are concerned with the effect of imposing rotation speeds inspired by the solution of the inviscid flow around the main body, and its impact on turbulent flow at $Re = 10^3$. This setup is compared with another, constrained to the same input kinetic energy, where all rods spin at an uniform rate. Hydrodynamic loads, wake dynamics and power expenditure are principally addressed.

From previous studies, the role of the individual control rods in vortex-shedding suppression is known to differ regarding their position relative to the main body and of their spinning motion. It is taken as a premise that an optimised setup will require different contributions from each rod,

thus it is of interest to comprehend if a potential-flow-inspired configuration may lead the system closer to an optimal operating condition.

2. Method

Figure 1 illustrates the object of this study: the main circular cylinder of diameter D is fitted with eight peripheral rods of diameter $d = D/20$, distanced by a gap $G = D/100$ from the central body. Angular velocities are denoted ω_n and $\omega'_n = -\omega_n$ ($n = 1$ to 4), corresponding, respectively, to the upper rods at positions P_n (that spin clockwise) and to the lower rods at P'_n (which rotate counter-clockwise). The entire system was subjected to an incoming flow of velocity U_∞. The rods were uniformly separated from each other and neither of them rested on the stagnation regions. The convention adopted for the angle θ, as displayed in figure 1, used a positive orientation clockwise with $\theta = 0^\circ$ at the frontal stagnation point.

The number of $N = 8$ control rods in this study followed the most successful configuration in VIV suppression found by Silva-Ortega and Assi (2017b). The selected gap was that of greatest mitigation of VIV response and drag carried out in the parametric study by Silva-Ortega and Assi (2017a). The chosen diameter d was based on the work of Assi et al. (2019), which produced enough interaction with the shear layers of the central body at a local low Re based on the rod diameter (also employed by Korkischko and Meneghini, 2012).

In the present work, two cases have been considered:

- **Case 0 - "uniform"**: All 8 rods were forced to rotate at the same angular velocity given by $|\omega_0|$ (considering their local clockwise and counter-clockwise directions). This case followed the approach employed by Assi et al. (2019), but with a different gap and flow regime.

- **Case 1 - "potential"**: The rods were forced to rotate at different angular velocities ω_n, specified in analogy to the solution of the potential flow over a bare cylinder, following Carvalho et al. (2021). The overall kinetic energy was the same as for case 0.

Rotation rates of case 1 were defined in the following manner: The velocity field from the potential flow about a plain cylinder was solved for positions $R = D/2 + G + d$ away from the axis of the main cylinder, as marked in figure 2a by small crosses. Consecutively, the rods were placed around the main body and the system was inserted in the turbulent flow at Reynolds number

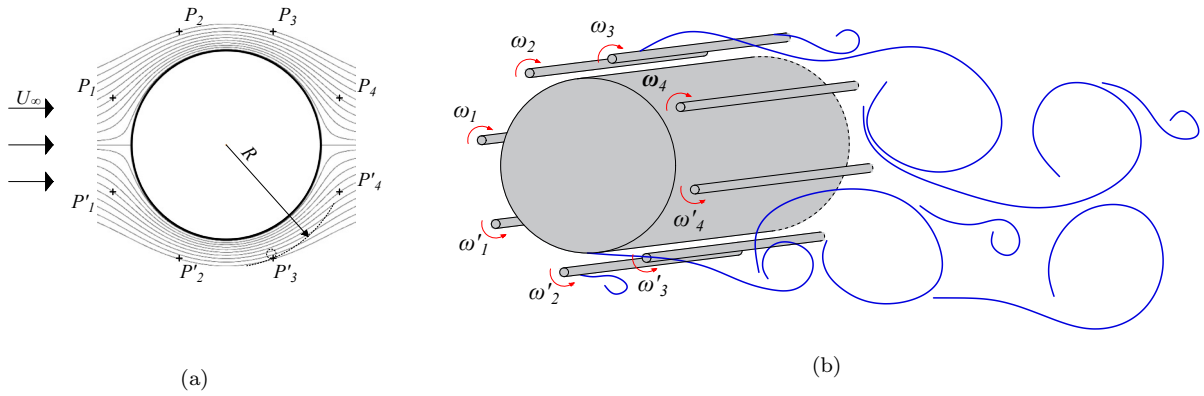

(a) (b)

Figure 2: (a) Streamlines of the potential flow around a bare cylinder providing velocity magnitudes at positions P_n. (b) The ratio between these velocities was imposed on case 1 to control the turbulent wake.

$Re = U_\infty D/\nu = 10^3$, where ν is the kinematic viscosity of the fluid and D is the diameter of the main body, as shown in figure 2b. Note that the wake becomes turbulent for $Re > 200$, as highlighted by Williamson and Roshko (1988).

In doing so, it was considered that: i) ω_n were set so that the input kinetic energy of cases 0 and 1 were the same for every ζ (defined later). ii) A fixed rotation ratio of $\omega_2/\omega_1 = \omega_3/\omega_4 = 2.41$ was determined by the potential flow around a bare cylinder, meaning that the tangential velocity on the spinning rod was that from the inviscid velocity field at the marked positions.

In order to spin all the rods faster at once, their angular velocities were multiplied by the parameter ζ, which varied from 0 to 5. For case 0, ζ directly represented the tangential velocities of all rods normalised by the far-field velocity, i.e., U_n/U_∞. More details on this potential analogy (in a laminar regime) are found in Carvalho et al. (2021).

2.1. Numerical scheme

The numerical scheme allowed for the resolution of the Navier-Stokes equations of momentum transport and the continuity equation, respectively given by

$$\rho\left(\frac{\partial U_i}{\partial t} + U_j\frac{\partial U_i}{\partial x_j}\right) = -\frac{\partial p}{\partial x_i} + \mu\frac{\partial^2 U_i}{\partial x_j \partial x_j}, \tag{1}$$

$$\frac{\partial U_j}{\partial x_j} = 0. \tag{2}$$

These equations were discretised and integrated over control volumes by means of the finite volume formulation. Simulations were carried out with the OpenFOAM library. The Eulerian

time-transient term was discretised with a fully implicit backward scheme. The divergence scheme was comprised of a blend made up of 25% of the linear upwind scheme and 75% of the central scheme. For turbulent quantities, the linear upwind scheme was used. Gradients were obtained from a cell-based least squares method. Laplacian terms were discretised according to unbounded Gauss theorem, together with linear interpolation. Correction for non-orthogonality (between a cell interface and the line connecting cell centres) was also applied. Discretisation of all the aforementioned terms involved second-order truncation error (Versteeg and Malalasekera, 2007).

For pressure-velocity coupling required in incompressible flows, the unsteady version of the SIMPLE algorithm (Patankar, 1980) was used for all simulations, and 10 corrector steps were considered without relaxation. The reference simulation of a plain cylinder was iterated to a maximum tolerance of 10^{-6} for the pressure. However, for the entire system of cases 0 and 1, a more relaxed 10^{-4} tolerance was imposed to the same field. These two levels of tolerance were simulated and generated the same results (omitted here for briefness), so for faster run times the 10^{-4} maximum residual was kept for the pressure. For all other fields, a 10^{-8} tolerance was met at the end of every time step.

Time steps were set to concomitantly capture at least 100 parts of the Strouhal period $T_S = (D/U_\infty)/St$ (where the Strouhal number $St \approx 0.2$ in sub-critical regime) and 70 parts of every revolution of the rods. In this matter, two points must be acknowledged: i) The small rods were on the threshold of vortex shedding (which occurs around $Re = 50$, precisely equal to the Reynolds related to the rods' diameter, $Re_d = Ud/\nu = 50$), therefore T_S is based on the main body. ii) *A priori*, it can be assured that for configurations with high rotation rates the three-dimensional, small-scale vortical flow structures were weakened as vortex shedding was suppressed, thus justifying the lower requirement for capturing the rotations.

Convergence was obtained for all simulations, and the last 30 cycles of vortex shedding were considered for mean and root mean square (RMS) computations. In order to comply with CFL conditions, the restrictive condition of a maximum Courant number of 0.98 was imposed. It was usually this condition that limited the time step sizes (over other less stringent time step conditions mentioned above).

It follows from the work of Carmo and Meneghini (2006) that 3D simulations are vital to properly incorporate the effects of vortical structures on the fluid loads for $Re > 190$. For cost-effective

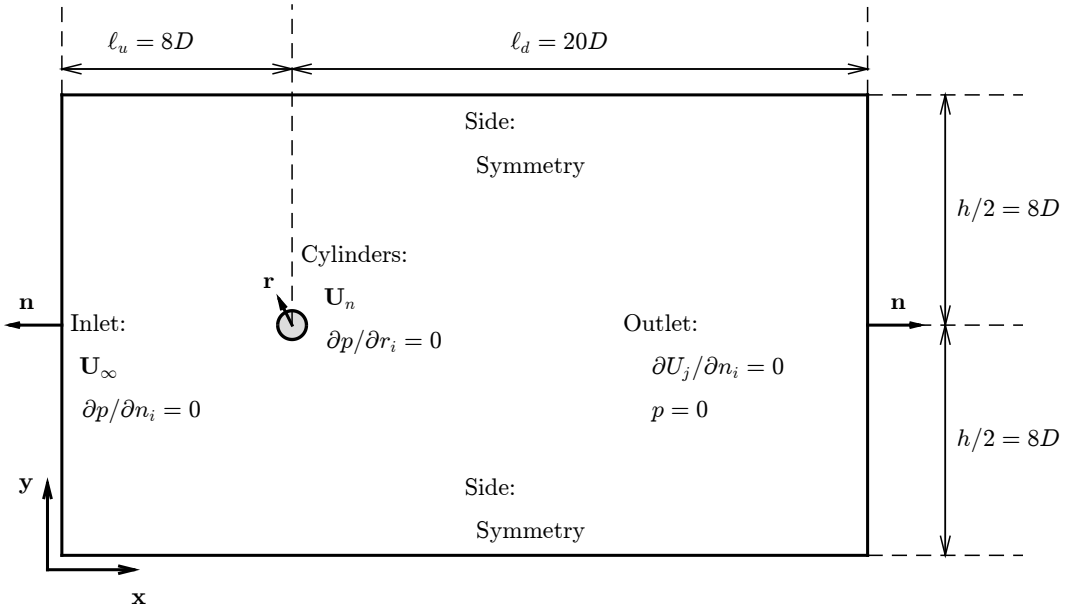

Figure 3: Flow domain and boundary conditions. Control rods are not represented for clarity.

3D simulations involving turbulence scales, the Detached Eddy Simulation (DES) formulation was elected (Spalart, 1997) for a good compromise between physical results and reasonable computational effort. This approach resolved the large (detached) eddies, while the boundary layer was modelled by means of the unsteady Reynolds-Averaged Navier-Stokes (URANS) equations. For small scales away from the boundary layer, the classical SGS model of Smagorinsky (1963) was used, whereas for the URANS-part, the one-equation model of Spalart and Allmaras (1992) allowed for the transport of the turbulent viscosity parameter and related it to the turbulent viscosity. Moreover, this model allowed to capture separation and reversed pressure gradient.

A major problem in the DES formulation for the flow about cylindrical structures in sub-critical regime is that the boundary layer is laminar whereas the wake is already turbulent (Williamson and Roshko, 1988), and the URANS formulation for the boundary layer is intrinsically turbulent. This downside was circumvented by a low-Reynolds correction (Spalart et al., 2006).

2.2. Boundary conditions and meshes

Boundary conditions are introduced schematically in figure 3 for the cross section ($x-y$ plane) of the extruded grid, both for the reference simulation of a plain cylinder and for the entire system.

Free stream velocity (uniform and constant) and zero pressure gradient were applied to the inlet; conversely, a Dirichlet condition was imposed to the outlet pressure, and Neumann's to the

Table 1: Grid information. The total number of cells corresponds to that resulting from the spanwise extrusion of the cross-sectional grid. The smallest element size relates to y^+.

	Number of cells		Smallest element
	Cross-section	Total	
Bare cylinder	49,204	2,361,792	$1.00 \times 10^{-3} D$
System	130,004	6,500,200	$1.54 \times 10^{-3} D$ (main body) $3.77 \times 10^{-3} d$ (control rods)

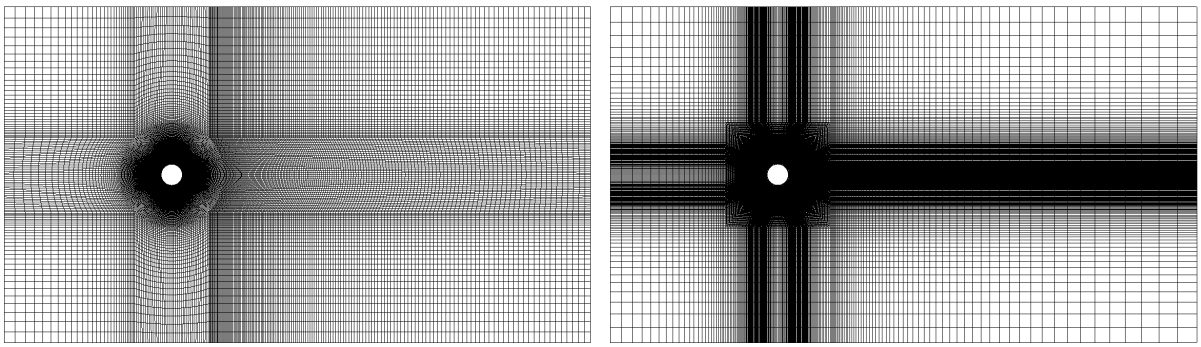

Figure 4: Grids used for the simulation of the bare cylinder (left) and of the entire system (right).

velocity. On the upper and lower sides, a symmetry condition prevailed. On the surface of the cylinders, the flow velocity matched the tangential velocity of the cylinders $U_n = \omega_n \, d/2$. Finally, the pair of front and back faces generated by the extrusion of the mesh (in the z-direction) were coupled by means of a periodic condition. The appropriate boundary conditions used for the turbulent quantities were those of Spalart (2000) and Vatsa et al. (2017), respectively, $\tilde{\nu}_{\text{wall}} = 0$ and $3 < \tilde{\nu}_\infty / \nu_\infty < 5$.

The structured meshes used in this work had lateral ($h/2$) and upstream (ℓ_u) boundaries distanced $8D$, and ample outflow distance $\ell_d = 20D$, away from the centre of the cylinder to avoid blockage effects (see figure 3). These values are in agreement with Behr et al. (1995, 1991). Sizes of the smallest elements – related to boundary layer refinement – sitting on the surfaces of the main body and rods are supported by table 1 along with further information. All simulations preserved $y^+ < 1$, the non-dimensional distance away from the walls of the cylinders. Figures 4 and 5 expose the cross-section of the meshes, focused on the fluid domain and on close-ups, respectively.

The meshes were extruded for a spanwise length $L = \pi D$ following Assi et al. (2018) for a

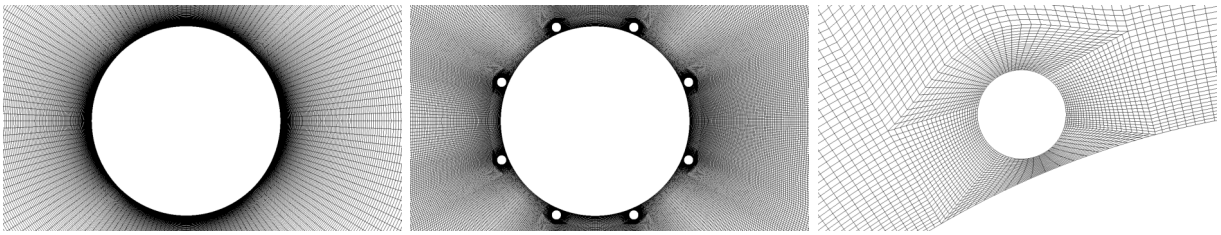

(a) (b) (c)

Figure 5: Close-up grids around (a) the bare cylinder, (b) the entire system, and (c) a control rod.

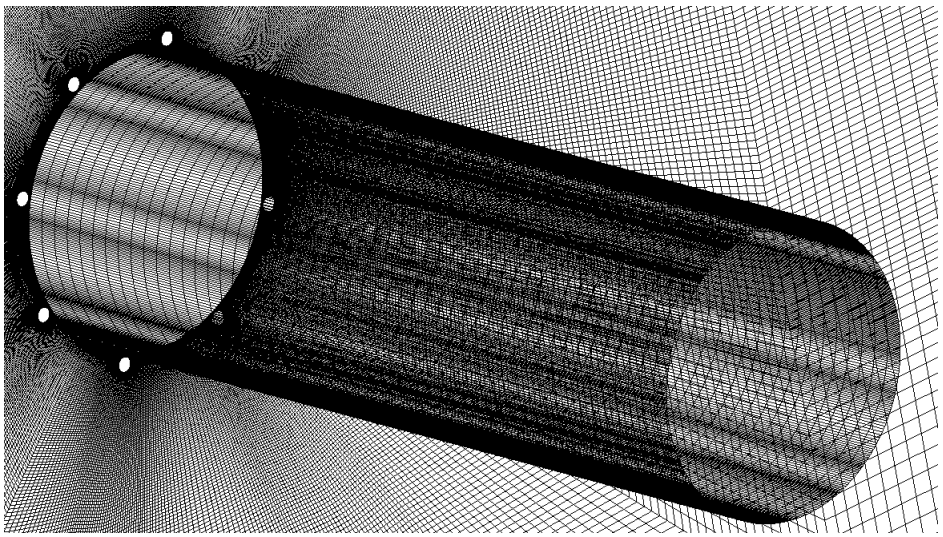

Figure 6: Extrusion of the grid. Only the main cylinder's extrusion is depicted for ease of visualisation.

system similar to the one here. The number of layers in this direction for the case of the plain cylinder (48) came from the work of Saltara et al. (2011). For the entire system 50 layers were used. Figure 6 portrays the extruded mesh (the extrusion of the rods is not represented for clarity).

2.3. Grid independence, verification and validation

Mesh convergence analysis, validation and verification procedures were performed for the reference case of a plain cylinder subjected to oncoming uniform flow at $Re = 10^3$. For the same Re, only mesh convergence was verified for the entire system. Simulations were conducted for at least $50T_S$ (for the more refined mesh), and $20T_S$ were awaited for convergence. Mean and RMS quantities were computed thereafter.

All meshes of table 2 were constrained to a first element of size $D/1000$ orthogonal to the

Table 2: Mesh convergence in terms of the mean drag ($\overline{C}_D$) and RMS of the fluctuating lift ($\hat{C}_L$). Percentages in parentheses refer to the comparison of a given mesh with the most refined one hereby analysed. Only the number of cells in the cross section (x-y plane) is disclosed, which was extruded for 48 layers in the spanwise z-direction.

Number	$Re = 10^3$		$Re = 10^4$	
of cells	$\overline{C}_D$	$\hat{C}_L$	$\overline{C}_D$	$\hat{C}_L$
27,854	1.00 (0.0%)	0.14 (16%)	1.10 (0.90%)	0.17 (19%)
39,224	1.00 (0.0%)	0.11 (8.3%)	1.13 (1.8%)	0.23 (9.5%)
49,204	1.00 (0.0%)	0.12 (0.0%)	1.11 (-)	0.21 (-)
67,504	1.00 (-)	0.12 (-)		

Table 3: Validation of the reference simulation of a bare cylinder. The maximum value of y^+ was 0.16.

	$\overline{C}_D$	$\hat{C}_L$	St
Jordan and Fromm (1972)	1.24		0.21
Braza et al. (1986)	1.1-1.2		0.21
Norberg (2001)		0.10-0.30	0.21
Cantwell and Coles (1983)	1.00		
Wieselsberger (1921)	1.00		
Present work (3D DES)	1.13	0.24	0.21

surface of the cylinder (as presented in table 1). It was noted that i) data displayed by tables 2 and 3 (the latter shall be discussed shortly) brought close values with mesh refinement. This was more pronounced for the mean drag ($\overline{C}_D$), which is of utmost interest to this paper, with variance below 3%. And ii) the mesh used in the work of Saltara et al. (2011) was coarser than the ones invested in this paper and they all shared the same size of the first cell near the wall. In view of these two remarks, we deem the present convergence analysis sufficient for the bare cylinder case and select the mesh with 49,204 elements as reference for the forthcoming comparisons.

Verification and validation of this mesh confirms through table 3 that the reference simulation agreed well with both numerical (first two references of the table) and experimental data (other references) in regard to mean drag ($\overline{C}_D$), RMS of the fluctuating lift ($\hat{C}_L$) and Strouhal number (St). Although $\overline{C}_D$ was a little overestimated when contrasted with experimental values, it agreed well with numerical works.

Table 4: Assessment of blockage effects for a wider flow domain.

ℓ_d/D	h/D	$\overline{C}_D$	$\hat{C}_L$	St	$y^+_{\max}$
20	16	1.13	0.24	0.22	0.16
30	32	1.08	0.22	0.22	0.15

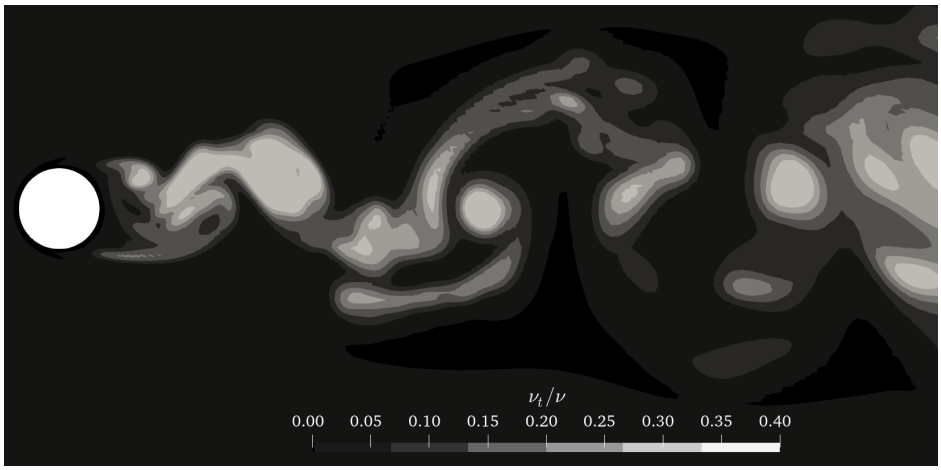

Figure 7: The ratio ν_t/ν shows a negligible value of ν_t near the wall and the expected wake transition downstream of the system.

Blockage effects were not extensively evaluated. Instead, results from previous studies concerned specifically with the adequate size of the domain (Behr et al., 1995, 1991) were used. The same simulation was run for a wider domain with $l_d/D = 30$ and $h/D = 32$. As table 4 points out, no significant difference was perceived.

The effect of the low-Re correction applied in this DES formulation became evident in light of figure 7, where a laminar boundary layer is revealed ($\nu_t/\nu \approx 0$), while transition to turbulence occurred downstream in the wake.

Additional simulations, omitted here for conciseness, were run the bare cylinder for $Re = 10^4$ and 10^6. We simply outline that the results, in terms of the featured quantities of table 3, corroborated to the validity of our meshing and numerical scheme.

For the entire system, only grid independence was investigated, due to the lack of data for this setup in the literature for validation and verification. The same numerical scheme and grid refinement were employed as in the simulations of the bare cylinder. As compiled by table 5, the results converged in terms of $\overline{C}_D$ and $\hat{C}_L$, with largest discrepancy between the more refined meshes

Table 5: Mesh convergence in terms of $\overline{C}_D$ and $\hat{C}_L$ for the entire system. Percentages in parentheses refer to the comparison of the respective mesh with the most refined grid hereby analysed. The number of cells in the cross section was extruded for 50 layers in the spanwise z-direction.

Number of cells (in the x-y plane)	$\overline{C}_D$	$\hat{C}_L$
53,632	1.79 (2.2%)	0.597 (3.5%)
61,828	1.87 (2.2%)	0.691 (12%)
99,092	1.87 (2.2%)	0.692 (12%)
130,004	1.83 (0.0%)	0.616 (0.44%)
150,544	1.83 (-)	0.618 (-)

just over 3%. In any simulation of this table, y^+ remained below 0.8 and Courant number below 0.99. The grid with 130,004 cells on the 2D plane (and 6,500,200 in total) was favoured for all simulations involving control rods. Results from a parallel grid evaluation, conducted in laminar regime for this same grid, supported the present analysis and agreed with the unstructured mesh of Carvalho et al. (2021) (suppressed here for conciseness).

3. Results

3.1. Effect of the control rods on vortex shedding

Simulations were run for 50 Strouhal periods (T_S) during each ζ-regime of cases 0 and 1, except for $\zeta = 0.0$ where $65T_S$ were considered. Transition from one regime to the next was allowed such that the flow field at the end of one simulation was mapped as startup for the subsequent one, thus providing lower iteration count at the beginning of each regime, as it was previously done by Mittal (2001). Time histories shown in figure 8 illustrate the effect of reducing both drag and lift coefficients as the control rods spun faster. Numerical transients at the start of the simulations were disregarded for mean and RMS computations. Figure 8 also highlights a distinctive aspect between the cases: The mean drag acting on the system in case 1 was clearly lower than in case 0, and vortex-shedding suppression was achieved with lower input kinetic energy in case 1 ($\zeta = 3.0$) compared with case 0 ($\zeta = 4.0$).

Figure 9 shows the wakes of the reference case (bare cylinder) and that of the system with

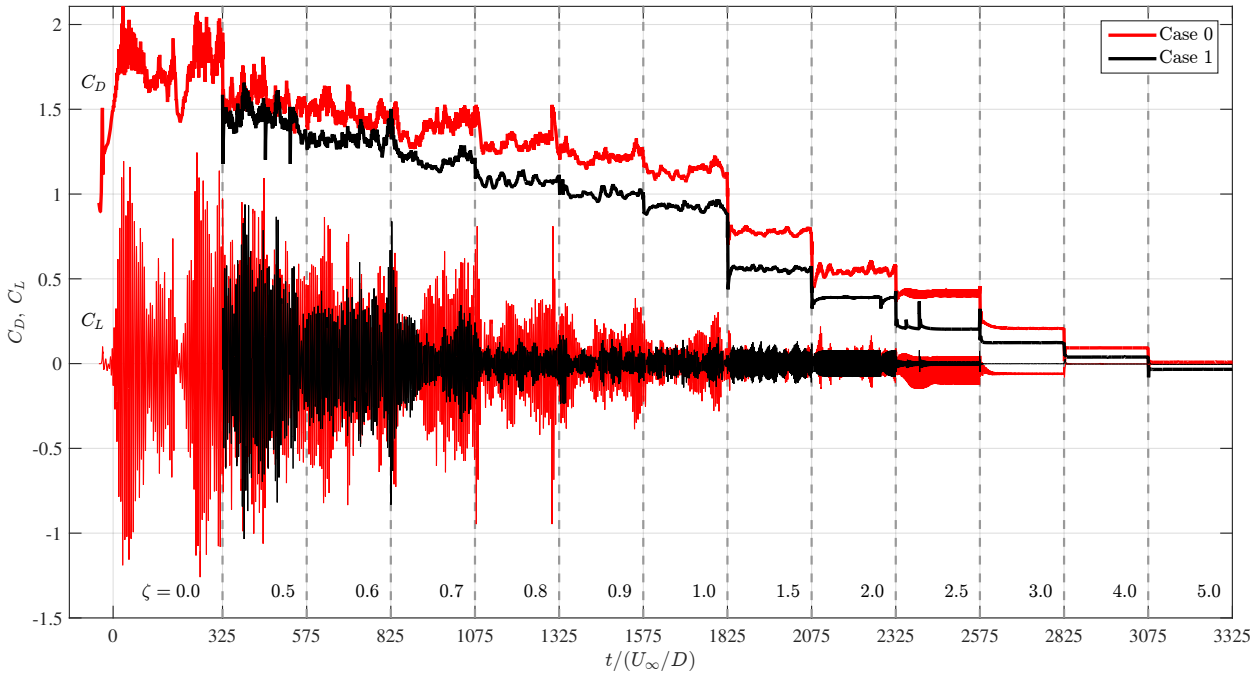

Figure 8: Time histories of lift (thin line) and drag (thick line) acting on the entire system for cases 0 and 1. Each rotation was run for $50T_S$. The different rotation regimes are distinguished by dashed vertical lines.

the peripheral devices in case 1 starting from a passive condition in which the rods were fixed, $\zeta = 0.0$, up to rotations able to suppress the vortex street, represented by $\zeta = 3.0$. Simply fitting the static control rods around the main cylinder produced a wider wake and the shortening of the vortex-formation length. Larger vortical structures were convected to the far wake when compared to the reference case, where smaller vortices were discernible downstream in figure 9.

However, as the rods started to spin, the wake narrowed from $\zeta = 1.0$ onwards and the vortex-formation region was elongated. Prolongation of the shear layers downstream led vortices to emanate farther away from the system. Consequently, the vortex wake lost strength due to viscous dissipation of vorticity concentrated in and carried by the shear layers.

Similar analyses to this one were made in laminar (Assi et al., 2019; Carvalho et al., 2021) and turbulent regimes (Assi et al., 2018). Strictly focused on the hereby denoted *case 0*, Assi et al. (2018) obtained reduction in vortex shedding at $Re = 10^4$, but did not suppress it.

The shedding frequency f_s, represented by the Strouhal number $St = f_S/(U_\infty/D)$ in figure 10, quantified the behaviour illustrated in figure 9. For $\zeta > 0.5$, St increased for both cases due to narrower wakes with longer vortex-formation lengths. As pointed out by Williamson (1996), St

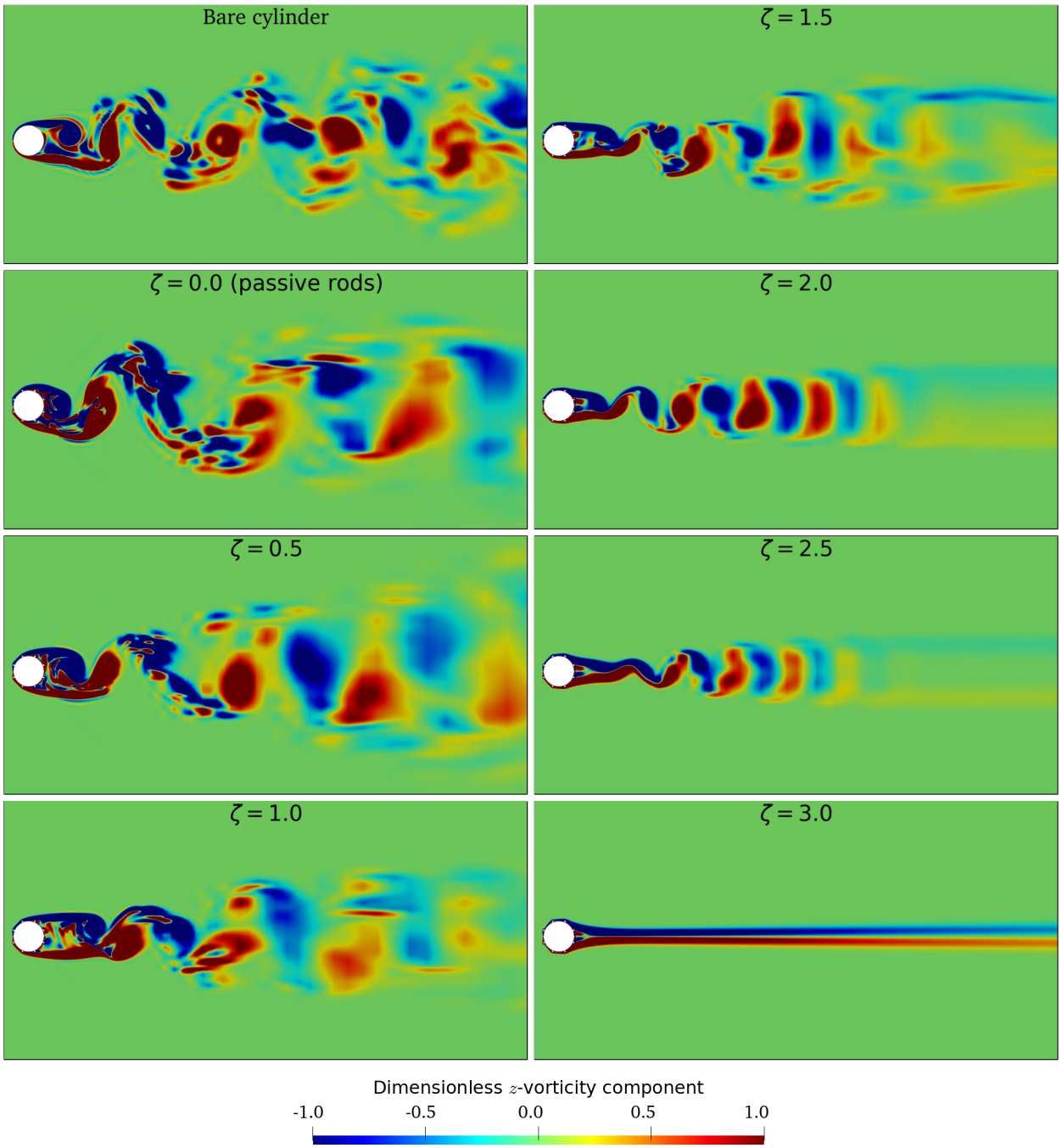

Figure 9: Contours of dimensionless z-vorticity component (normalised by U_∞/D) for the reference case (head figure) and for the system with wake-control rods of case 1.

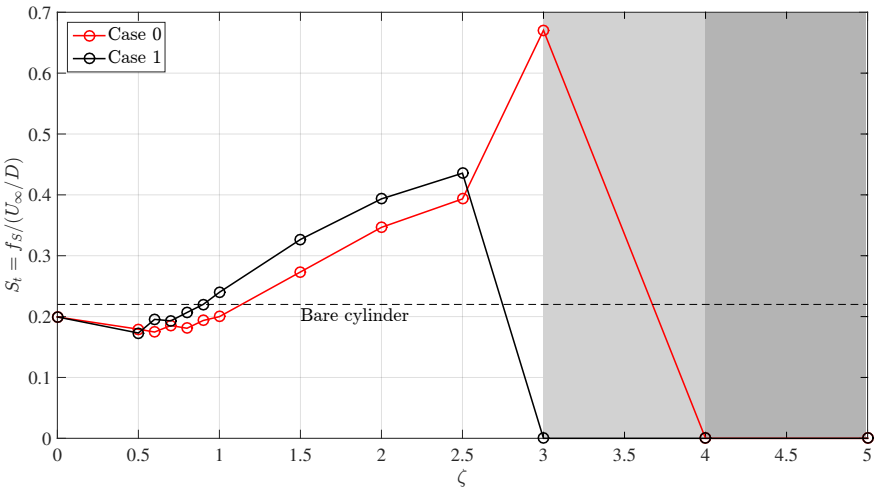

Figure 10: Variation of the dimensionless frequency with angular velocities. The onset of suppression for case 1 is represented by the lighter shading, while the darker one corresponds to that of case 0.

scales inversely with wake width and formation length. As ζ approached 0.9, St for the entire system of case 1 approached that for a bare cylinder, whereas for case 0 this only happened after $\zeta = 1.0$. This increase of shedding frequency was detected up to $\zeta = 3.0$, and $\zeta = 2.5$, respectively, for cases 0 and 1.

A steeper rise of St occurred in case 0 beyond $\zeta = 2.5$, reaching $St \approx 0.67$ for $\zeta = 3.0$. For $\zeta \geq 4.0$ vortex shedding was completely suppressed producing $St = 0$, which is marked by the dark-grey area in the plot. Case 1 achieved vortex suppression ($St = 0$) for $\zeta \geq 3.0$, marked by the light-grey area figure 10. Perhaps a sharp increase of St could also have been found for case 1 if another data point were produced between $\zeta = 2.5$ and 3.0. Vortex shedding is not expected to return for ζ higher than these critical values.

3.2. Active control of the three-dimensional wake

Figure 11 presents a three-dimensional visualisation of the turbulent structures in the flow by means of the Q-criterion (following Hunt et al., 1988, here $Q = 0.1$). A gradient ranging from black to white points to the relative importance of the turbulent viscosity against the molecular one, ν_t/ν. Firstly, the figure recalls the aspect portrayed by figure 9, i.e., vortex-shedding suppression. Secondly, transition of the wake past the system stands out, highlighting white-coloured eddies (greater ν_t/ν) being formed closer to the system with the passive mechanism, compared with the reference case. At the same time, the presence of smaller structures away from the system was

reduced.

One must bear in mind that, with the presence of the passive rods, the wake was correspondingly shortened lengthwise, so turbulence was produced earlier. However, as the rods started to spin, turbulence was dissipated, as shown by the white-coloured eddies gradually fading into black and ν_t/ν approached 0. As a matter of fact, $\zeta = 1.5$ depicted the suppression of almost all small-scale turbulent structures, and anticipated the highly correlated, two-dimensional flow condition verified for $\zeta \geq 2.0$. Higher rotation speeds achieved complete suppression of vortex shedding; at $\zeta = 3.0$ the Q-contours were only marginally visible in the neighbourhood of the rods. Suppression of vortex shedding was verified for ζ up to 5.0, not shown here for briefness.

Vortex dynamics is further illustrated in figure 12 for case 1 configurations in which the rods were progressively rotated at $\zeta = 0.0$, 1.0, 2.0 and 2.5. The summary of this figure is that with faster spinning of the rods, the wake transitioned from a rich three-dimensional state to another stated dominated by coherent, two-dimensional vortex tubes (succeeded by complete suppression verified for $\zeta = 3.0$, not shown in this figure). For the four ζ-regimes in each column, the evolution of a vortex tube can be followed in time through the white stars as it is convected downstream from the body (grey body on the left of each snapshot).

Beyond this general description, two others aspects are worth attention. The first is that for $\zeta = 0.0$ and $\zeta = 1.0$, respectively, the first and second columns of figure 12 capture an easily-presumed spectral distribution of a turbulent wake, represented by the smaller scales in the near wake in random-like motion, promptly dissipated; and larger scales in the far wake, travelling in close alignment with the free stream direction. Of course, the colour gradient announces a vorticity distribution that is also within expectation. Ranging from blue to red (see colour key), it depicts respectively, low to high vortical content found, correspondingly, in large to small scales.

The second aspect is that $\zeta = 2.0$ allows one to appreciate a different wake development (third column of figure 12). As the vortices were convected downstream, *'vortex dislocations'* were observed. These vortex structures reminded the wake dynamics associated with the *mode B* instability, as denoted by Williamson (1996), with "finer-scale streamwise vortices". In their formation, a downstream row of vortices feeds back on the upstream row by means of these *vortex pairs* until their elimination by viscous dissipation. This mechanism of vorticity transfer between streamwise vortices can be seen in figure 13, reminiscent of the direct simulation of Zhang et al.

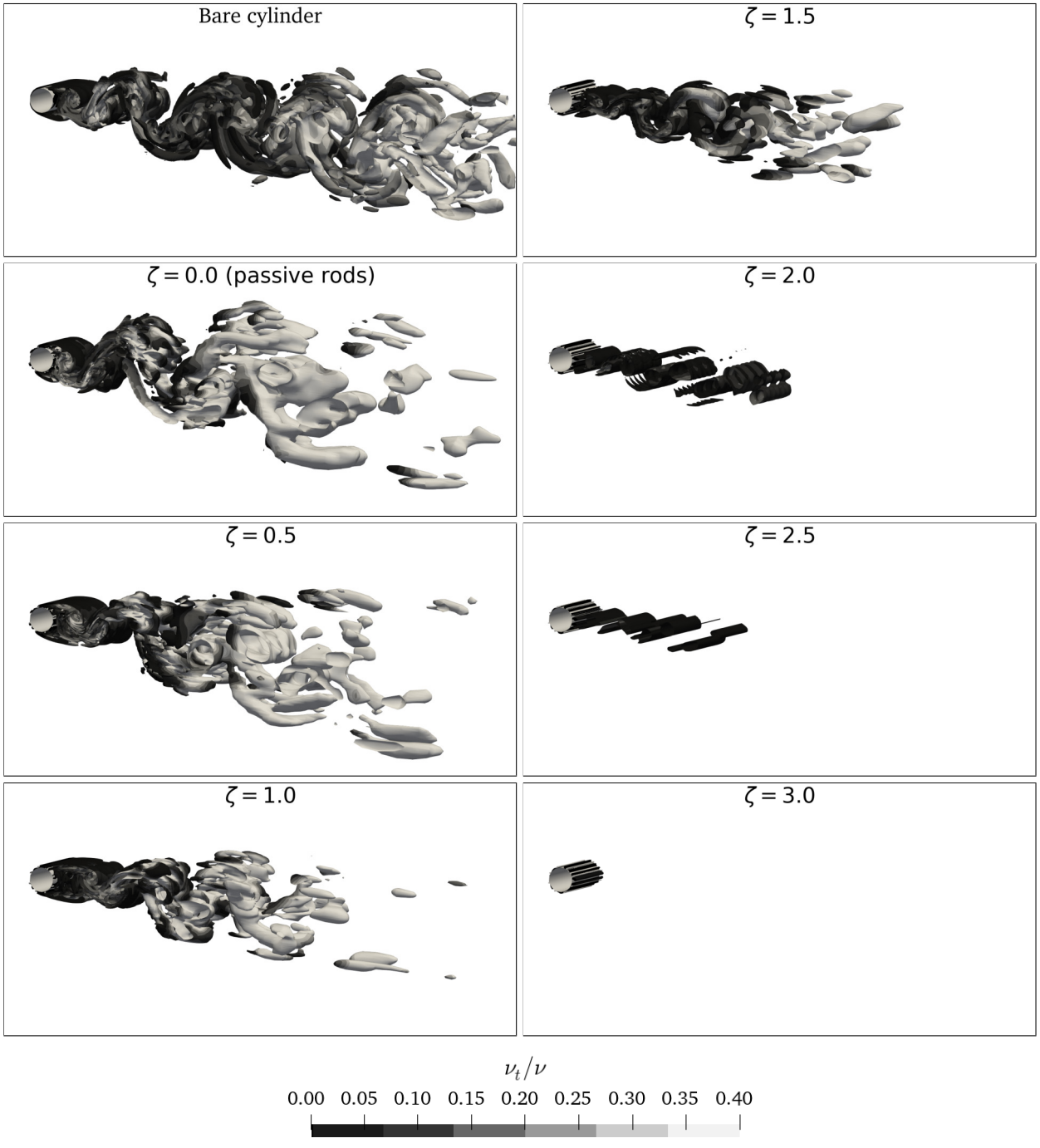

Figure 11: Q-criterion for vortex visualisation of case 1. Contours of $Q = 0.1$ are coloured according to ν_t/ν. From the passive ($\zeta = 0.0$) to the most active mechanism ($\zeta = 3.0$) the mitigation of turbulent structures becomes evident.

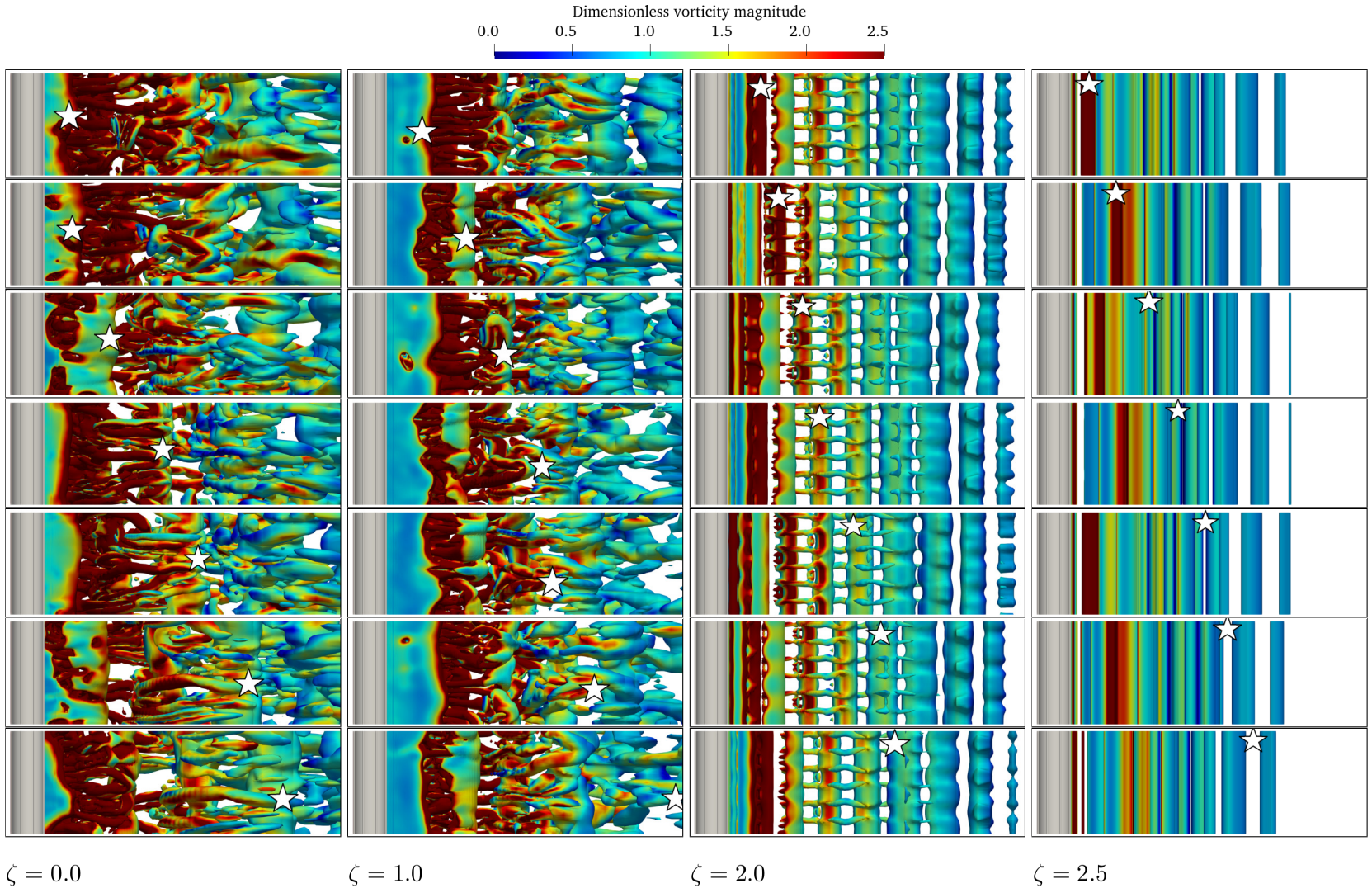

Figure 12: Q-contours ($Q = 0.1$) coloured by dimensionless vorticity magnitude (normalised by U_∞/D). From left to right, the columns corresponding to ζ show progressive organisation of the wake. From top to bottom, the white stars mark the motion of a typical turbulent structure travelling downstream in time (snapshots were taken at unequal time intervals).

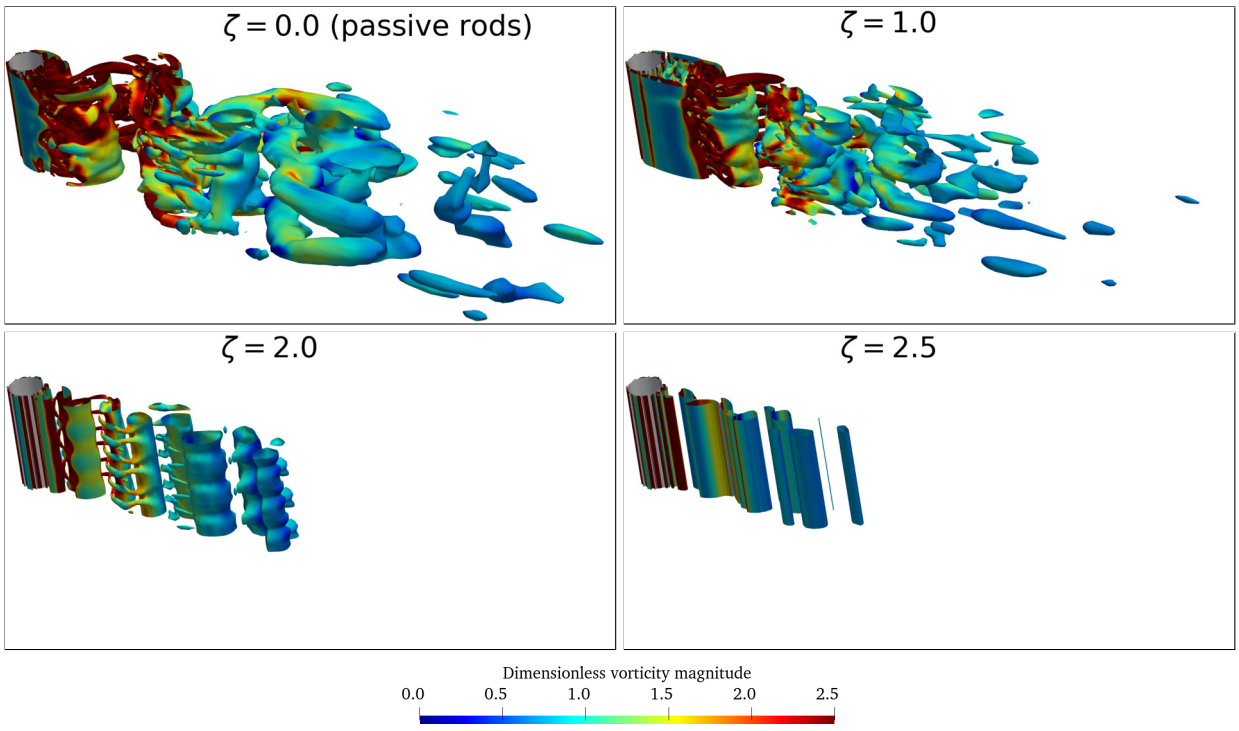

Figure 13: Vortices shed by the system underwent progressive organisation and elimination of small turbulence scales as the rods spun faster. $\zeta = 2.0$ instigated the occurrence of *mode B* (Williamson, 1996) and triggered the formation of *vortex pairs* as a means of vorticity transfer between rows of vortices.

(1995) apud Williamson (1996).

Interestingly, Williamson (1996) located this topology in the *wake-transition regime* of a bare cylinder ($230 \leq Re \leq 250$) with spanwise wavelength of the order of $1D$, whereas the present results were obtained on the intersection with a *shear-layer transition regime* ($10^3 \leq Re = 2 \times 10^5$) with wavelength of about $0.7D$. Longer formation length than that of Unal and Rockwell (1988) would be expected in the reference case for the same Re, but the opposite is observed here for the entire system (figure 14). Also in opposition is the growing St, as previously verified in figure 10. This pattern of streamwise vortices was not observed earlier for systems such as the present.

It appears that the rods effectively "lower the Re-regime". For the present flow regime they not only prevented shear layer transition, but also wake transition, given enough power input. High ζ-regimes resemble the visual character of low-Re flow past circular cylinders.

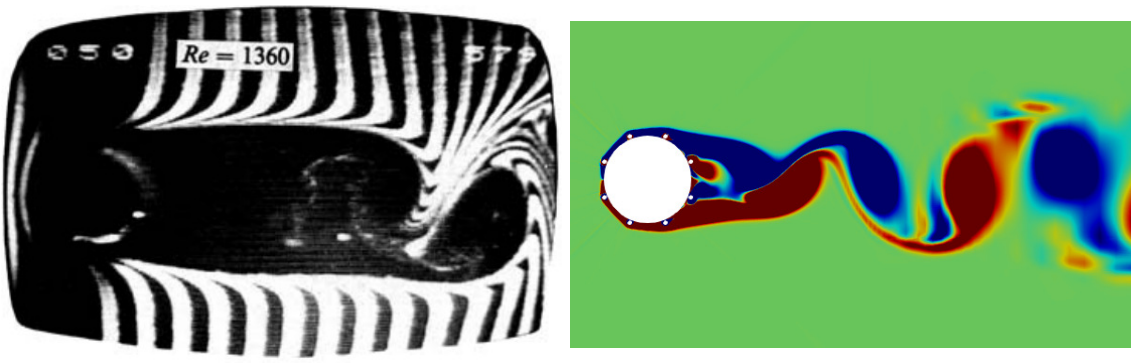

(a) (b)

Figure 14: Control rods alter the Re-regime and its corresponding wake features. Both figures (a) at $Re = 1360$ from Unal and Rockwell (1988) and (b) the present case at $Re = 1000$ refer to sub-critical regime, and yet show different formation lengths.

3.3. Decrease in hydrodynamic loads

Mean drag and RMS of the fluctuating lift on the peripheral rods altogether, on the main cylinder and on the entire system are presented in figure 15. The rods behaved collectively oblivious to the shift from the setup of case 0 to the potential-flow-inspired case 1, aside from the following nuances: higher $\overline{C}_D$ (less negative) in case 1 for $\zeta \geq 2.0$, and lower $\hat{C}_L$ in case 1 for $0.5 \leq \zeta \leq 1.0$ and $2.0 \leq \zeta \leq 4.0$.

In contrast, the analysis differs for the main cylinder and for the entire system: The new setup (case 1) reduced mean drag for the entire ζ-range. As for the lift, case 1 was either comparable to case 0 ($\zeta = 1.5$ and 2.0) or presented lower $\hat{C}_L$ (other values within $\zeta \geq 0.5$). A rather curious deviation from sheer decay in case 0 took place in $\hat{C}_L$, at $\zeta = 0.7$ (see figure 15b). This was previously reported in Assi et al. (2018) (there, also in regard to $\overline{C}_D$) and invites further investigation. Incidentally, it was at this value of ζ for the main cylinder of case 1 that $\overline{C}_D = 1.16$ roughly equalled the baseline case and $\hat{C}_L = 0.059$ was lower.

We now focus on the loads acting on the entire system. An increase in the angular speeds to $\zeta = 2.5$ led to merely residual vortex-shedding for case 1 accompanied by almost zero fluctuating lift, whereas for case 0 there was a rise in the $\hat{C}_L$ that gradually fell to 0 as ζ approached 4.0. Figure 15 also renders three further remarks: i) A setup with $\zeta = 0.7$ already attenuated $\hat{C}_L$ to approximately half of the value of the reference case (figure 15b), while $\overline{C}_D$ remained virtually at the same value (1.19 against 1.13, see figure 15a). A similar behaviour was observed for case 0

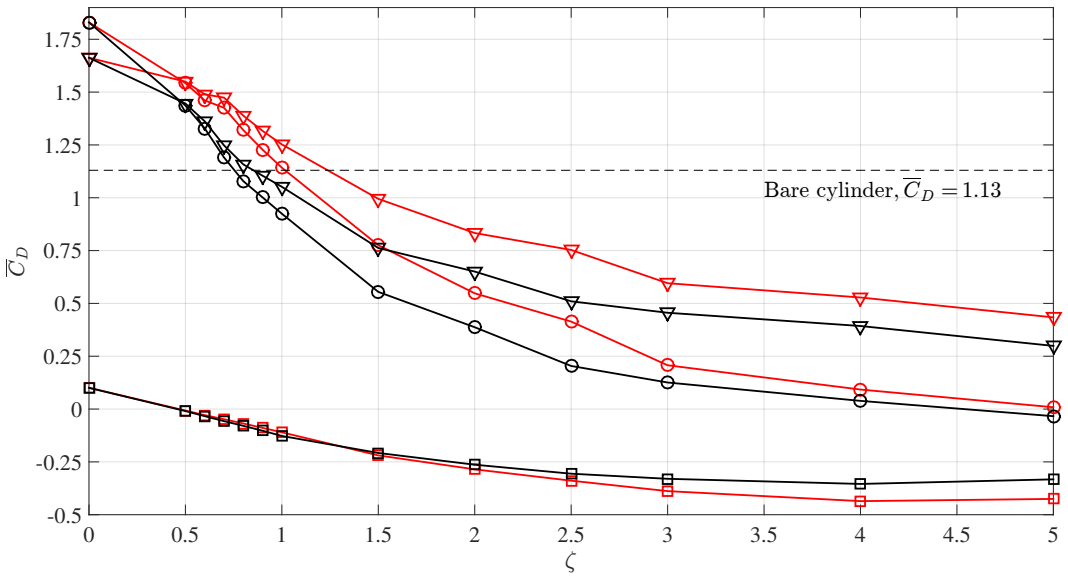

(a) Mean drag ($\overline{C}_D$).

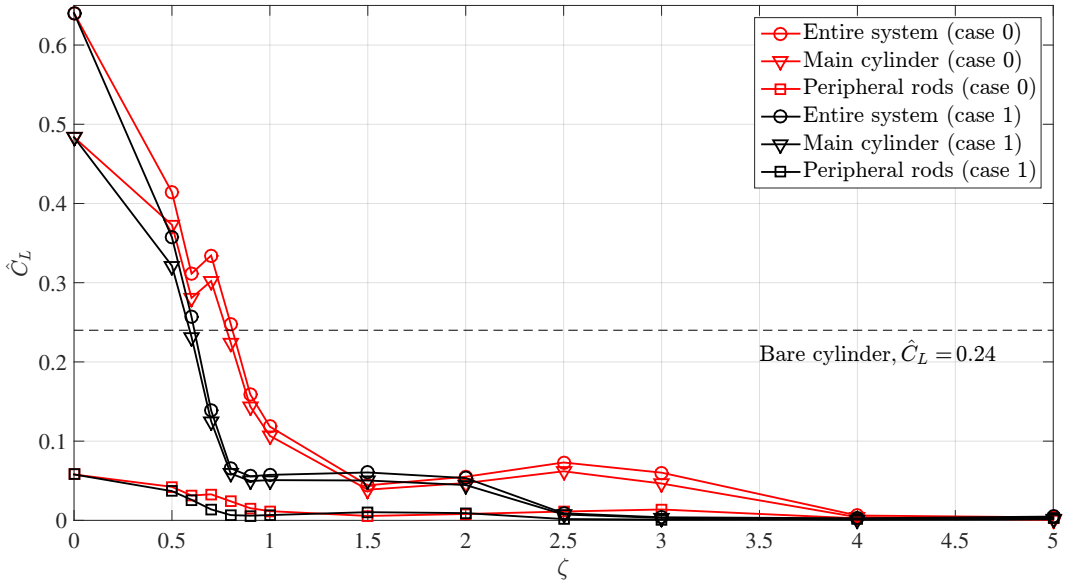

(b) Root mean square (RMS) of the fluctuating lift ($\hat{C}_L$).

Figure 15: (a) Mean drag and (b) RMS of the fluctuating lift on the entire system, on the main cylinder and that resulting from the collective effect on the peripheral rods.

only after $\zeta = 1.0$; ii) Suppression of vortex shedding was succeeded by complete elimination of the mean drag at the upper end of the ζ range. ii) Sufficient rotation of the control rods slightly inverted the drag and thus produced thrust on the entire system, as verified for $\zeta = 5.0$ with $\overline{C}_D = -0.034$. For the present system, drag inversion was previously observed only for laminar regimes (Assi et al., 2019).

3.4. Resultant forces

Now our attention is directed to the total force applied on every rod of case 1. Figure 16 represents only the upper part of the entire system, since the other half is symmetric by design. In this figure, the radial forces are probably due to the Magnus effect, as the spinning motion altered the pressure distribution on the surface of the rotating rods. The figure schematically reveals that the strongest individual contributions (coloured arrows) distinctly came from the intermediate rods P_2 and P_3, followed in much less magnitude by P_1 and P_4. Departing from the reference case, one might argue that P_1 was located close to a stagnation region, and P_4 was placed within the wake, hence their lower contributions to wake control (Cicolin et al., 2021). Contrarily, P_2 and P_3 strongly interacted with the separation region, comprehended between them (Thompson and Hourigan, 2005; Cao et al., 2010), as they surrounded the (upper) 'shoulder' of the bluff body. Moreover, P_2 and P_3 interacted with the incipient shear layer. Therefore, P_2 and P_3 bore most of the hydrodynamic loads supported by the rods to control the wake that would otherwise form between them, and they further displaced the separation point aft the entire system.

Furthermore, drag inversion is apparent for P_2 and P_3 in figure 16. Propulsion of P_1 and P_2 developed with sufficient angular velocity, and led to an imbalance between left- (P_1 and P_2) and right-meridian (P_3 and P_4) rods in terms of streamwise force component. Eventually, this difference built up into thrust on the entire system, as can be interpreted from the respective arrows in greyscale acting on the main body. For this range of values of ζ, the same phenomenon was not exhibited by case 0 (as shown in figure 15a). For both main cylinder and the entire system, the magnitude of the resultant force was reduced with larger ζ. It is interesting to note, from figures 15a and 16, that a negative $\overline{C}_D$ was obtained for the entire system of case 1 when $\zeta = 5.0$ (shown by a small reversed arrow in figure 16), meaning that so much energy was put into the system to generate a small propulsion on the system. This phenomenon was also observed in the experimental investigation performed by Silva-Ortega and Assi (2017a) at moderate Re.

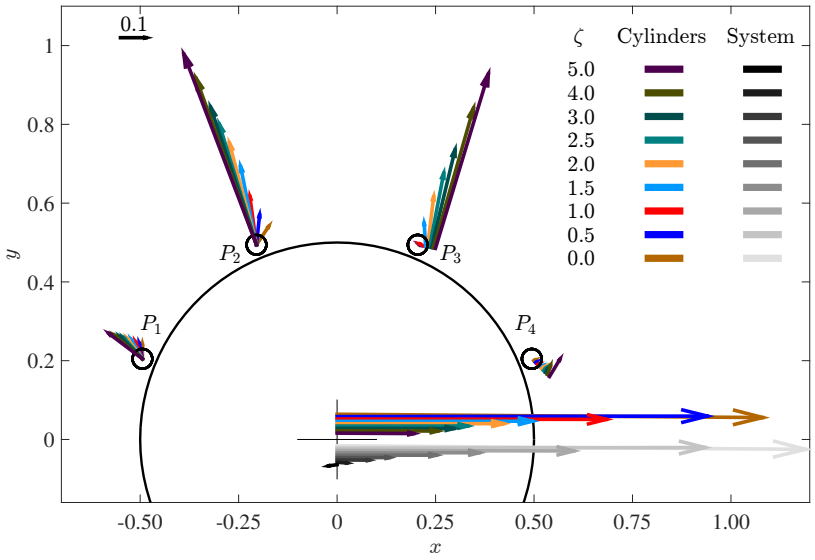

Figure 16: Resultant forces acting on each cylinder (coloured) and on the entire system (gray) of case 1 for $\zeta = 0$ to 5.0. The radial vectors were deliberately moved from the axis of their respective cylinders whenever necessary for better visualisation. On the upper left, 0.1 unit of non-dimensional force is exemplified.

Of course, considerations made here also apply to the symmetrical counterparts, i.e., P_1', P_2', P_3' and P_4' and the same behaviour was followed in case 0 (not shown here for briefness).

This result is aligned with the similar numerical study at laminar-flow regime by Carvalho et al. (2021), inasmuch as with other works in laminar and turbulent regimes that comprised analysis only of what is denoted here *case 0* (Assi et al., 2019, 2018). Notwithstanding the confirmation of these papers, the present result further corroborates with previous hypothesis of Carvalho et al. (2021) whether a potential-inspired setup could indeed lead to the decrease in hydrodynamic loads even in turbulent regime. Indeed, the above discussion positively supports that idea.

Figure 17 shows that case 1 produced more intense loads on the intermediate cylinders in comparison to case 0. Indeed, these cylinders responded to a much stronger combination of lift and drag in case 1 than in case 0; the greater the value of ζ, the greater was the difference between the cases. On the other hand, end rods of case 1 faced ever less representative loads relative to case 0, despite their gradual increase. For P_4, the results are in agreement with the work of Cicolin et al. (2021) for the main cylinder, even though the negative drag reported by these authors was not detected here. This may be justified in view of the different Re ranges, as well as on account of the near-rod flow dynamics resulting from the spinning effect, not present in Cicolin et al. (2021).

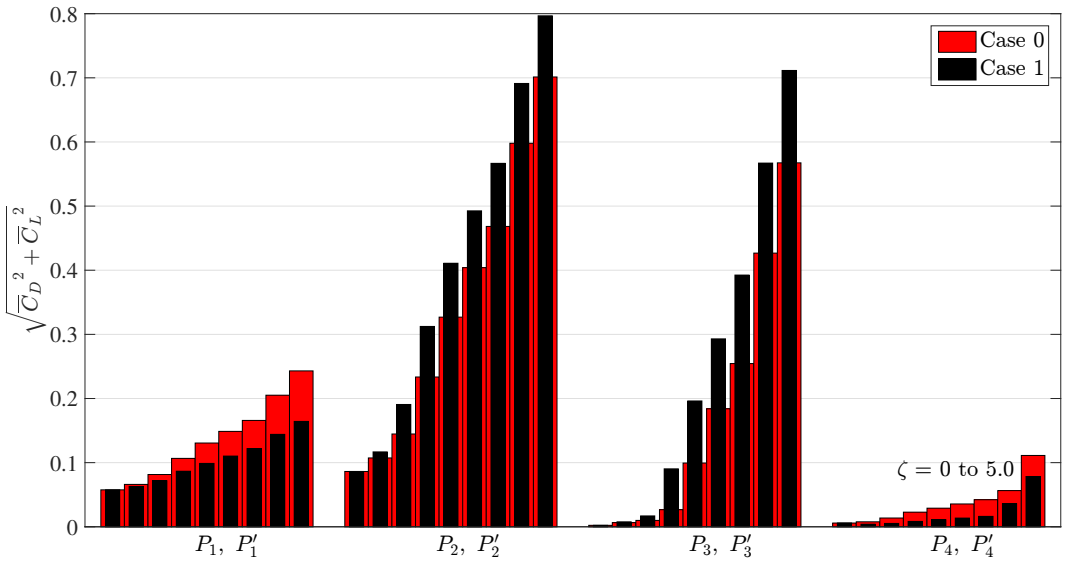

Figure 17: Variation of the resultant force acting on each rod with increasing angular velocities, for $\zeta = 0.0$, 0.5, 1.0, 1.5, 2.0, 2.5, 3.0, 4.0 and 5.0.

It is now of interest to examine how longitudinal and transverse components of these loads impacted every rod for higher rotation rates.

3.5. Individual and collective contributions of the control rods

Mean drag and lift coefficients are referred to in figure 18 for every rod. The angle θ is associated to the frontal stagnation region and its positive orientation is given clockwise (as indicated in figure 1), such that opposing rods are marked by opposite angles, e.g., P_1 ($\theta = 22.5°$) and P_1' ($\theta = -22.5°$), etc.

First and foremost, the figure ascertains expected behaviours from theory and previous works, such as the symmetry in mean drag (figure 18a) and antisymmetry in mean lift (figure 18b) provided by opposing rods. The general growth in magnitude can also be noted (Assi et al., 2019; Carvalho et al., 2021). Short variation in drag and lift for the end rods, and correspondingly wider change for the intermediate ones with ζ quantitatively substantiate the overall discussion of the past section.

Another aspect brought by this figure is the inversion of mean drag with an increase in ζ. This occurred for rods P_2, P_2' and P_3, P_3' (figure 18a). For the former pair of symmetrically-positioned rods, this was observed for the change in ζ from 0.5 to 1.0 and for the entire range of ζ the mean drag decreased monotonically. For the latter pair, drag inversion took place in the transition from $\zeta = 1.5$ to 2.0, and absolute values of mean drag did not match a monotonic tendency; they

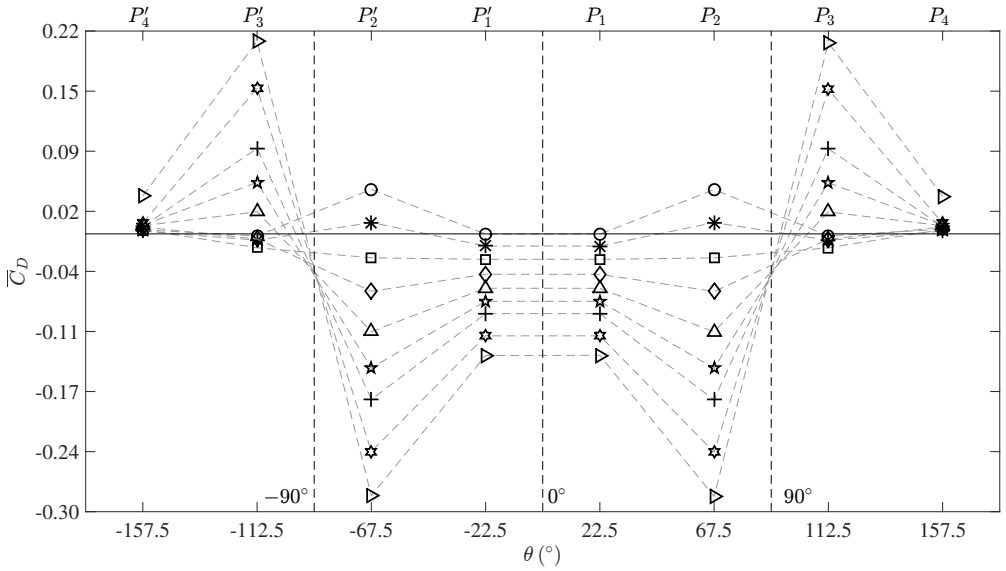

(a) Mean drag on each rod.

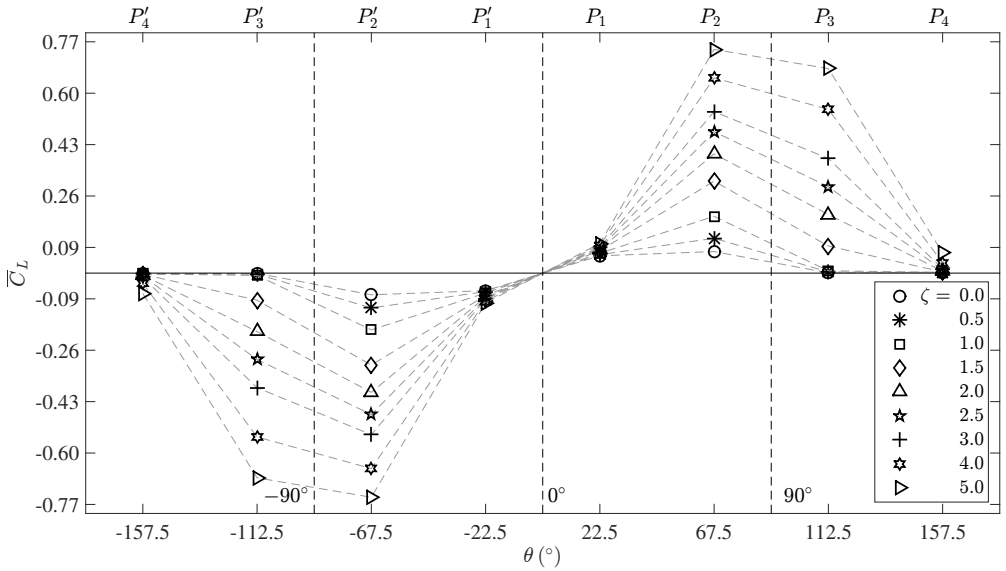

(b) RMS of the fluctuating lift on each rod.

Figure 18: Mean drag (a) and RMS of the fluctuating lift (b) on control rods varying ζ. General monotonic tendencies followed $\zeta > 1.0$.

rather followed a descending trend between $\zeta = 0.0$ and 1.0. Outside of these intervals, $\overline{C}_D$ values accompanied ascending trends for ever greater values of ζ: P_1, P_1' and P_2, P_2' adopted negative, while P_3, P_3' and P_4, P_4' led to progressively positive values.

As expected, the rods were insensitive to the suppression of vortex shedding of the entire system in both cases, since no alteration was noted in mean drag or lift past the corresponding ζ. The Reynolds number based on the rods' diameter was merely $Re_d = 50$, on the brink of vortex shedding. Even if vortices were shed from the fixed rods for such small Re_d, the rotation would have eliminated this phenomenon at its root. Asymmetry produced by rotation of the cylinder was suggested as a means of attaining a steady wake in Badr et al. (1990).

3.6. Power expenditure

Both circulation and injection of momentum resulting from the placement of the spinning elements surrounding the main body resulted in power expenditure required by MSBC. Following the formulation proposed by Shukla and Arakeri (2013), the power-loss coefficient, given in time-averaged form by

$$\overline{C}_{PL} = \overline{C}_D + \overline{C}_N, \tag{3}$$

quantifies the effort made by the control system to attenuate mean drag, $\overline{C}_D$, and to counteract shear forces on the $N = 8$ rotating rods

$$C_N = \sum_{n=1}^{N} \frac{p_n}{\rho U_\infty^3 D/2}, \tag{4}$$

in which

$$p_n = U_n \int_0^{2\pi} \tau_n(\theta)\ \frac{d}{2}\ \mathrm{d}\theta, \tag{5}$$

where $\tau_n(\theta)$ and U_n correspond, respectively, to the shear stress over the surface of the n-th rod and U_n to its tangential velocity. Overlined quantities indicate time-averaging (as described in section 2).

Figure 19 presents $\overline{C}_{PL}$ and its components, $\overline{C}_N$ and $\overline{C}_D$. Shaded areas demarcate the region of complete elimination of vortex shedding, highlighting an earlier occurrence in case 1. The figure anticipates the more power-demanding feature of this new setup, as the curve of $\overline{C}_N$ surpassed that of $\overline{C}_D$ at $\zeta = 1.67$ and 1.38 for cases 0 and 1, respectively.

It becomes evident that in either case, the value of the power-loss coefficient was never below that of the mean drag of the reference case. This contrasts with the previous study of Carvalho et al.

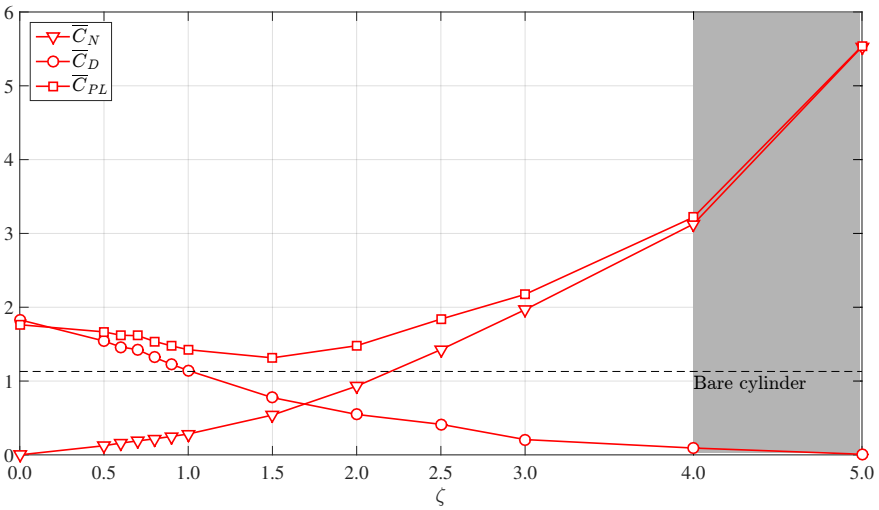

(a) Case 0.

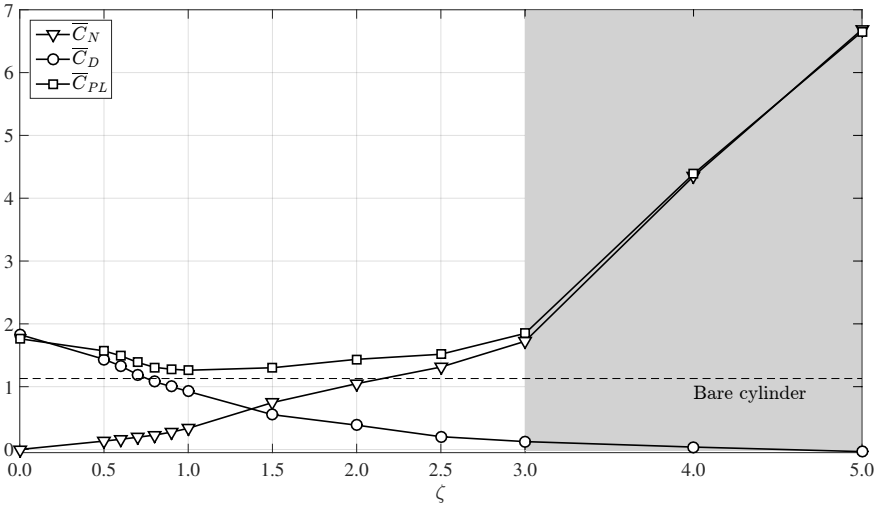

(b) Case 1.

Figure 19: Mean values of the total power-loss coefficient ($\overline{C}_{PL}$) and of its constituents – power-loss due to shear ($\overline{C}_N$) and to drag ($\overline{C}_D$) – for cases 0 and 1. Shading indicates regions of vortex-shedding suppression.

(2021) in laminar regime, where C_{PL} found lower values than $\overline{C}_D$ of a plain cylinder. Additional data are required in figure 19 to understand if such an event could happen between $\zeta = 1.0$ and 1.5 in case 1, but an educated guess likely points otherwise. Even in the occurrence of such an event, suppression of vortex shedding would not have been attained within this interval of ζ.

In a suppressed-wake condition, comparison against the reference case of a bare cylinder shows that the ratio $(\overline{C}_{PL}/\overline{C}_{D,\text{Bare}})_{\text{case 0}} = 2.85$ at $\zeta = 4.0$, and $(\overline{C}_{PL}/\overline{C}_{D,\text{Bare}})_{\text{case 1}} = 1.63$ at $\zeta = 3.0$, proving the more efficient suppression of vortex shedding provided in case 1. Another aspect that must be retrieved here is that for the same ζ, cases 0 and 1 spent the same input kinetic energy. This enhances the appeal to case 1 for cost-effective vortex-shedding suppression, since $\zeta = 4.0$ required more kinetic energy than $\zeta = 3.0$.

Finally, figure 20 presents the components of $\overline{C}_{PL}$. Dotted vertical lines indicate where the wake was already suppressed. In terms of drag reduction, at the same ζ, case 0 reduced the mean drag to 0.092 (at $\zeta = 4.0$), whereas case 1 reached 0.13 (at $\zeta = 3.0$). This shows a downside of the new configuration for the incipient elimination of the vortex formation (although at lower requirement of input kinetic energy). Comparison of $\overline{C}_D$ and $\overline{C}_N$ outlined in the figure highlights that any suppressed condition demanded power expenditure. Furthermore, the frontier $\overline{C}_D = \overline{C}_N$ divides the figure into drag- and shear-dominated regions. At higher ζ, $\overline{C}_N$ dominated the composition of $\overline{C}_{PL}$ as it can be promptly noted for $\zeta = 5.0$. Unless propulsion is desired, started for $\zeta = 5.0$ in case 1, limiting $\zeta < 5$ as in the scope of this work aptly fulfills the purpose of suppression of vortex shedding with drag reduction.

4. Conclusion

A system comprised of a main cylinder fitted with 8 rotating peripheral rods distanced radially by a gap from the central body was analysed in this paper. DES simulations were conducted in turbulent regime at $Re = 10^3$. Two cases were assessed: case 0, where all rods adopted a uniform absolute speed value $|\omega_n|$; and case 1, where the angular velocities ω_n of the rods were inspired by potential-flow theory, thus weighting the relative position of the rods. The two cases were constrained to the same input kinetic energy. The parameter ζ multiplied the speed of all rods at once to evaluate the effect of the active devices for different rotation rates.

Vortex dynamics showed that the use of the potential-flow-inspired system produced a more

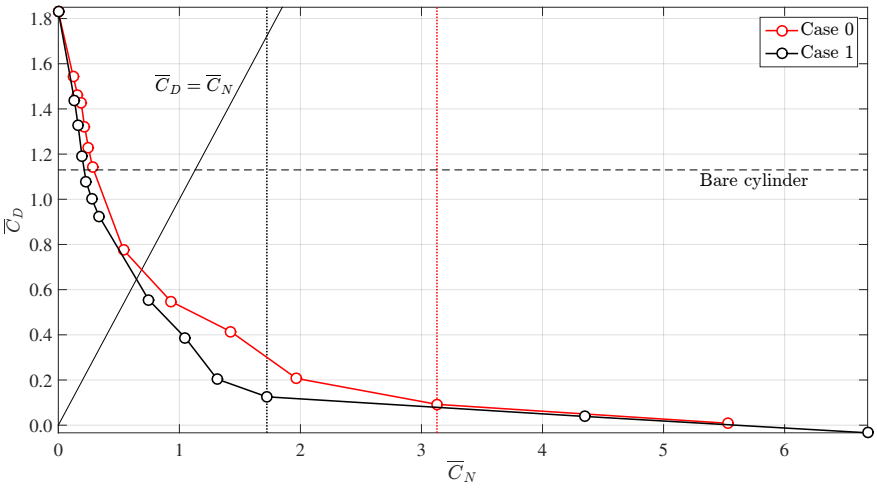

Figure 20: $\overline{C}_D$ vs $\overline{C}_N$. Dotted vertical lines point to the onset of a controlled, steady-wake condition.

effective way to mitigate vortex shedding. In general, mean drag ($\overline{C}_D$) and RMS of the fluctuating lift ($\hat{C}_L$) acting upon the entire system were significantly reduced using the new configuration compared with the uniform setup. This result was associated with a narrower wake and an elongated formation length, leading to increased shedding frequency prior to the transition of the wake to a steady condition.

Besides, it was demonstrated by means of Q-contours of turbulent viscosity that the spinning rods led to a two-dimensional "laminarised" state of the flow, that progressively eliminated turbulent structures. *Vortex dislocations*, in the sense of the vortex-shedding *mode B* of vorticity transfer were detected streamwise, provided the system was supplied with enough actuating power (sufficiently high ζ). One might wonder whether the spinning rods' effect was to "lower the effective Re-regime", taking in consideration that mode B was reported by Williamson (1996) in a wake-transition regime, rather than in a sub-critical regime as in the present work.

Although the loads acting on the group of rods made up by P_n (or, alternatively, by P'_n) seemed insensitive to the distinction between cases 0 and 1, analysis of the individual contributions of the rods showed preference of case 1 to concentrate the effort on the intermediate rods (P_2 and P_3) more intensely than in case 0 for greater ζ, discerning case 1 from case 0 in greater power expenditure. Nevertheless, this behaviour at the upper limit of the velocities hereby analysed was offset by lower $\hat{C}_L$ and $\overline{C}_D$ throughout most ζ-regimes and a more efficient control of the wake. Indeed, because the end rods (P_1 and P_4) were located near stagnation regions, they were expected to interact less

with boundary and shear layers. Hence, case 1 anticipated vortex-shedding suppression relative to case 0, thus required lower input kinetic energy and actuating power to control the vortex street.

Concerning the entire system, the present study showed that the power-loss coefficient (that includes power spent to counteract shear and effort to reduce drag) – resulting either from the new configuration or from the uniform-speed one – was not enough to lower the power-loss coefficient below the value of the mean drag of the reference case of a plain cylinder (a contrast with the result at a laminar regime found by Carvalho et al., 2021).

Finally, we were able to show that potential-flow-inspired angular velocities are effective even in turbulent, three-dimensional regime to reduce hydrodynamic loads, and beyond, to suppress vortex shedding entirely. Future work should concern with the system free to respond to vortex-induced vibrations and with multi-objective optimisation of the angular velocities.

Acknowledgments

IAC is grateful to CAPES Brazilian Ministry of Education for his PhD scholarship and to the National Laboratory for Scientific Computing (LNCC/MCTI, Brazil) for providing HPC resources of the SDumont supercomputer. GRSA acknowledges the support of FAPESP, Brazil (2011/00205-6) and CNPq, Brazil (306146/2019-3). We gratefully acknowledge the support of the RCGI Research Centre for Greenhouse Gas Innovation, hosted by the University of São Paulo, Brazil and sponsored by FAPESP (2020/15230-5) and Shell Brasil.

References

Assi, G.R.S., Orselli, R.M., Silva-Ortega, M., 2018. Suppression of vortex shedding with rotating wake-control cylinders: Numerical investigation at a moderate reynolds number, in: International Conference on Offshore Mechanics and Arctic Engineering, American Society of Mechanical Engineers. p. V002T08A060.

Assi, G.R.S., Orselli, R.M., Silva-Ortega, M., 2019. Control of vortex shedding from a circular cylinder surrounded by eight rotating wake-control cylinders at Re= 100. Journal of Fluids and Structures 89, 13–24.

Badr, H.M., Coutanceau, M., Dennis, S.C.R., Menard, C., 1990. Unsteady flow past a rotating circular cylinder at reynolds numbers 103 and 104. Journal of Fluid Mechanics 220, 459–484.

Behr, M., Hastreiter, D., Mittal, S., Tezduyar, T., 1995. Incompressible flow past a circular cylinder: dependence of the computed flow field on the location of the lateral boundaries. Computer Methods in Applied Mechanics and Engineering 123, 309–316.

Behr, M., Liou, J., Shih, R., Tezduyar, T., 1991. Vorticity-streamfunction formulation of unsteady incompressible flow past a cylinder: Sensitivity of the computed flow field to the location of the outflow boundary. International Journal for Numerical Methods in Fluids 12, 323–342.

Braza, M., Chassaing, P.H.H.M., Minh, H.H., 1986. Numerical study and physical analysis of the pressure and velocity fields in the near wake of a circular cylinder. Journal of fluid mechanics 165, 79–130.

Cantwell, B., Coles, D., 1983. An experimental study of entrainment and transport in the turbulent near wake of a circular cylinder. Journal of fluid mechanics 136, 321–374.

Cao, S., Ozono, S., Tamura, Y., Ge, Y., Kikugawa, H., 2010. Numerical simulation of reynolds number effects on velocity shear flow around a circular cylinder. Journal of Fluids and structures 26, 685–702.

Carmo, B.S., Meneghini, J.R., 2006. Numerical investigation of the flow around two circular cylinders in tandem. Journal of Fluids and Structures 22, 979–988.

Carvalho, I.A., Assi, G.R.S., Orselli, R.M., 2021. Wake control of a circular cylinder with rotating rods: Numerical simulations for inviscid and viscous flows. Journal of Fluids and Structures 106, 103385.

Choi, H., Jeon, W.P., Kim, J., 2008. Control of flow over a bluff body. Annu. Rev. Fluid Mech. 40, 113–139.

Cicolin, M.M., Buxton, O.R.H., Assi, G.R.S., Bearman, P.W., 2021. The role of separation on the forces acting on a circular cylinder with a control rod. Journal of Fluid Mechanics 915.

Fujarra, A.L.C., Rosetti, G.F., de Wilde, J., Gonçalves, R.T., 2012. State-of-art on vortex-induced motion: A comprehensive survey after more than one decade of experimental investigation, in: Proceedings of the OMAE International Conference on Offshore Mechanics and Arctic Engineering, pp. 561–582.

Gerrard, J.H., 1966. The mechanics of the formation region of vortices behind bluff bodies. Journal of fluid mechanics 25, 401–413.

Gonçalves, R.T., Rosetti, G.F., Fujarra, A.L.C., Nishimoto, K., 2011. An Overview of Relevant Aspects on VIM of Spar and Monocolumn Platforms. Journal of Offshore Mechanics and Arctic Engineering 134. 014501.

Hunt, J.C.R., Wray, A., Moin, P., 1988. Eddies, stream, and convergence zones in turbulent flows. Studying Turbulence Using Numerical Simulation Databases-I1 193.

Jordan, S.K., Fromm, J.E., 1972. Oscillatory drag, lift, and torque on a circular cylinder in a uniform flow. The Physics of Fluids 15, 371–376.

Korkischko, I., Meneghini, J., 2012. Suppression of vortex-induced vibration using moving surface boundary-layer control. Journal of Fluids and Structures 34, 259–270.

Mittal, S., 2001. Control of flow past bluff bodies using rotating control cylinders. Journal of fluids and structures 15, 291–326.

Mittal, S., Raghuvanshi, A., 2001. Control of vortex shedding behind circular cylinder for flows at low Reynolds numbers. International Journal for Numerical Methods in Fluids 35, 421–447.

Modi, V., Fernando, M.S.U.K., Yokomizo, T., 1990. Drag reduction of bluff bodies through moving surface boundary layercontrol, in: 28th Aerospace Sciences Meeting, p. 298.

Norberg, C., 2001. Flow around a circular cylinder: aspects of fluctuating lift. Journal of fluids and structures 15, 459–469.

Patankar, S.V., 1980. Numerical heat transfer and fluid flow.

Patino, G.A., Gioria, R.S., Meneghini, J.R., 2017. Evaluating the control of a cylinder wake by the method of sensitivity analysis. Physics of Fluids 29, 044103. doi:10.1063/1.4979482, arXiv:https://doi.org/10.1063/1.4979482.

Saltara, F., Neto, A., Lopez, J., et al., 2011. 3D CFD simulation of vortex-induced vibration of cylinder. International Journal of Offshore and Polar Engineering 21.

Shukla, R.K., Arakeri, J.H., 2013. Minimum power consumption for drag reduction on a circular cylinder by tangential surface motion. Journal of Fluid Mechanics 715, 597–641. doi:10.1017/jfm.2012.537.

Silva-Ortega, M., Assi, G., 2017a. Suppression of the vortex-induced vibration of a circular cylinder surrounded by eight rotating wake-control cylinders. Journal of Fluids and Structures 74, 401 – 412.

Silva-Ortega, M., Assi, G.R.S., 2017b. Flow-induced vibration of a circular cylinder surrounded by two, four and eight wake-control cylinders. Experimental Thermal and Fluid Science 85, 354 – 362.

Smagorinsky, J., 1963. General circulation experiments with the primitive equations: I. the basic experiment. Monthly weather review 91, 99–164.

Spalart, P., 2000. Trends in turbulence treatments, in: Fluids 2000 conference and exhibit, p. 2306.

Spalart, P., Allmaras, S., 1992. A one-equation turbulence model for aerodynamic flows, in: 30th Aerospace Sciences Meeting and Exhibit, p. 439.

Spalart, P.R., 1997. Comments on the feasibility of les for wings, and on a hybrid rans/les approach, in: Proceedings of first AFOSR international conference on DNS/LES, Greyden Press.

Spalart, P.R., Deck, S., Shur, M.L., Squires, K.D., Strelets, M.K., Travin, A., 2006. A new version of detached-eddy simulation, resistant to ambiguous grid densities. Theoretical and computational fluid dynamics 20, 181–195.

Strykowski, P.J., Sreenivasan, K.R., 1990. On the formation and suppression of vortex shedding at low reynolds numbers. Journal of Fluid Mechanics 218, 71–107.

Thompson, M.C., Hourigan, K., 2005. The shear-layer instability of a circular cylinder wake. Physics of Fluids 17, 021702.

Unal, M.F., Rockwell, D., 1988. On vortex formation from a cylinder. part 1. the initial instability. Journal of Fluid Mechanics 190, 491–512.

Vatsa, V.N., Lockard, D.P., Spalart, P.R., 2017. Grid sensitivity of SA-based Delayed-Detached-Eddy-Simulation model for blunt-body flows. AIAA Journal 55, 2842–2847.

Versteeg, H.K., Malalasekera, W., 2007. An introduction to computational fluid dynamics: the finite volume method. Pearson education.

Wieselsberger, C., 1921. Recent statements on the laws of liquid and air resistancy. Phys. Z 22, 321–328.

Williamson, C.H., Roshko, A., 1988. Vortex formation in the wake of an oscillating cylinder. Journal of fluids and structures 2, 355–381.

Williamson, C.H.K., 1996. Vortex dynamics in the cylinder wake. Annual review of fluid mechanics 28, 477–539.

Williamson, C.H.K., Govardhan, R., 2004. Vortex-induced vibrations. Annu. Rev. Fluid Mech. 36, 413–455.

Zdravkovich, M.M., 1981. Review and classification of various aerodynamic and hydrodynamic means for suppressing vortex shedding. Journal of Wind Engineering and Industrial Aerodynamics 7, 145–189.

Zhang, H.Q., Fey, U., Noack, B.R., König, M., Eckelmann, H., 1995. On the transition of the cylinder wake. Physics of Fluids 7, 779–794.

Corrigendum to "Enhanced control of the turbulent flow past a circular cylinder with rotating rods inspired by an inviscid solution" [J. Fluids Struct. 113 (2022) 1-21]

I. A. Carvalho[a,*], G. R. S. Assi[b]

[a] *Department of Mechanical Engineering, EPUSP, University of São Paulo, Brazil*
[b] *Department of Naval Architecture & Ocean Engineering, EPUSP, University of São Paulo, Brazil*

In Carvalho and Assi (2022) a normalization factor was missed. Instead of computing C_N per unit length, given by

$$C_N = \sum_{n=1}^{N} \frac{p_n}{\rho U_\infty^3 DL/2} \tag{1}$$

we computed, incorrectly,

$$C_N = \sum_{n=1}^{N} \frac{p_n}{\rho U_\infty^3 D/2}. \tag{2}$$

Thus, C_N, computed by equation 2 in the paper, was overestimated. It was computed as if it were for a body of spanwise length πD (matching the spanwise length employed in our grid and simulations), instead of per unit length, as it should, following the approximation of an infinitely-long body, which was used throughout the paper. As a consequence, the power-loss coefficient per unit length, given by $\overline{C}_{PL} = \overline{C}_D + \overline{C}_N$ involved an incorrect and overestimated value for $\overline{C}_N$. We apologise to the reader for the inconvenience. The revised sections 3.6 with the correct computation of C_N, and section 4 with the adjusted conclusions are presented below. In actuality, the system functioned more efficiently than formerly addressed.

3.6. Power expenditure

Both circulation and injection of momentum resulting from the placement of the spinning elements surrounding the main body resulted in power expenditure required by MSBC. Following the formulation proposed by Shukla and Arakeri (2013), the power-loss coefficient, given in time-averaged form by

$$\overline{C}_{PL} = \overline{C}_D + \overline{C}_N, \tag{3}$$

*Corresponding author: amorim.icaro@usp.br (I. A. Carvalho)
DOI of original article: https://doi.org/10.1016/j.jfluidstructs.2022.103652

Published article (in its final form: September, 2023):
Carvalho, I. A., and G. R. S. Assi. "**Corrigendum to "Enhanced control of the turbulent flow past a circular cylinder with rotating rods inspired by an inviscid solution" [J. Fluids Struct. 113 (2022) 1-21**" Journal of Fluids and Structures 122 (2023):103978. **https://doi.org/10.1016/j.jfluidstructs.2023.103978**

quantifies the effort made by the control system to attenuate mean drag, $\overline{C}_D$, and to counteract shear forces on the $N = 8$ rotating rods

$$C_N = \sum_{n=1}^{N} \frac{p_n}{\rho U_\infty^3 DL/2}, \tag{4}$$

in which

$$p_n = U_n \int_0^{2\pi} \tau_n(\theta)\ \frac{d}{2}\ \mathrm{d}\theta, \tag{5}$$

where $\tau_n(\theta)$ and U_n correspond, respectively, to the shear stress over the surface of the n-th rod and U_n to its tangential velocity. Overlined quantities indicate time-averaging (as described in Section 2 of the paper).

Figure 19 presents $\overline{C}_{PL}$ and its components, $\overline{C}_N$ and $\overline{C}_D$. Shaded areas demarcate the region of complete elimination of vortex shedding, highlighting an earlier occurrence in case 1. The figure anticipates the more power-demanding feature of this new setup, as the curve of $\overline{C}_N$ surpassed that of $\overline{C}_D$ at $\zeta = 2.42$ and 2.10 for cases 0 and 1, respectively.

It becomes evident that in both cases, the value of the power-loss coefficient was below that of the mean drag of the reference case for a range of values (as in Carvalho et al., 2021, in laminar regime). In case 0 this occurred between $\zeta = 1.18$ and 4.06, while in case 1 the same happened within $\zeta = 0.835$ and 3.60.

In a suppressed-wake condition, comparison against the reference case of a bare cylinder shows that the ratio $(\overline{C}_{PL}/\overline{C}_{D,\mathrm{Bare}})_{\mathrm{case\ 0}} = 0.963$ at $\zeta = 4.0$, and $(\overline{C}_{PL}/\overline{C}_{D,\mathrm{Bare}})_{\mathrm{case\ 1}} = 0.596$ at $\zeta = 3.0$, proving the more efficient suppression of vortex shedding provided in case 1. Another aspect that must be retrieved here is that for the same ζ, cases 0 and 1 spent the same input kinetic energy. This enhances the appeal to case 1 for cost-effective vortex-shedding suppression, since $\zeta = 4.0$ required more kinetic energy than $\zeta = 3.0$.

Finally, figure 20 presents the components of $\overline{C}_{PL}$. Dotted vertical lines indicate where the wake was already suppressed. In terms of drag reduction, at the same ζ, case 0 reduced the mean drag to 0.092 (at $\zeta = 4.0$), whereas case 1 reached 0.13 (at $\zeta = 3.0$). This shows a downside of the new configuration for the incipient elimination of the vortex formation (although at lower requirement of input kinetic energy). Comparison of $\overline{C}_D$ and $\overline{C}_N$ outlined in the figure highlights that a suppressed condition may be achieved without additional power-loss. Moreover, a steady condition was achieved with lower power loss than that by mean drag of a bare cylinder, proving

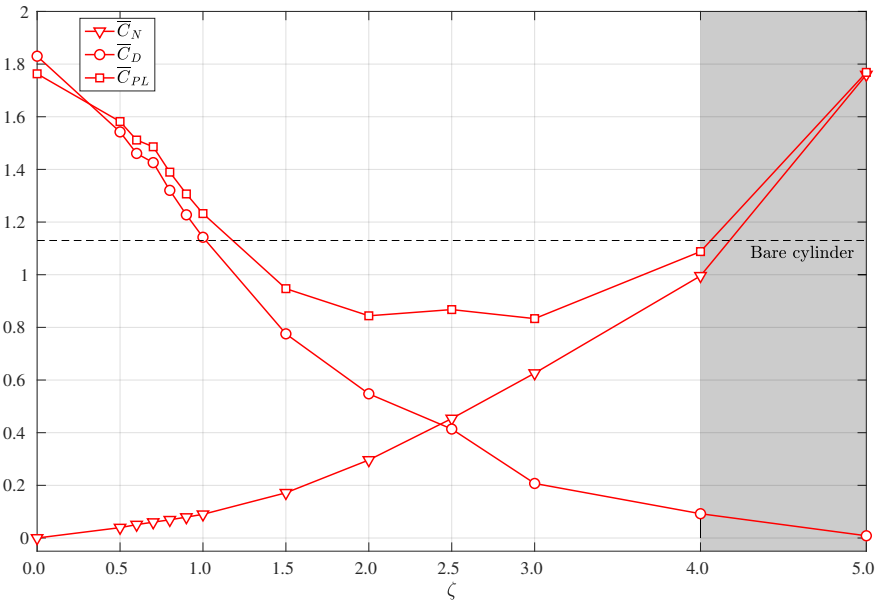

(a) Case 0.

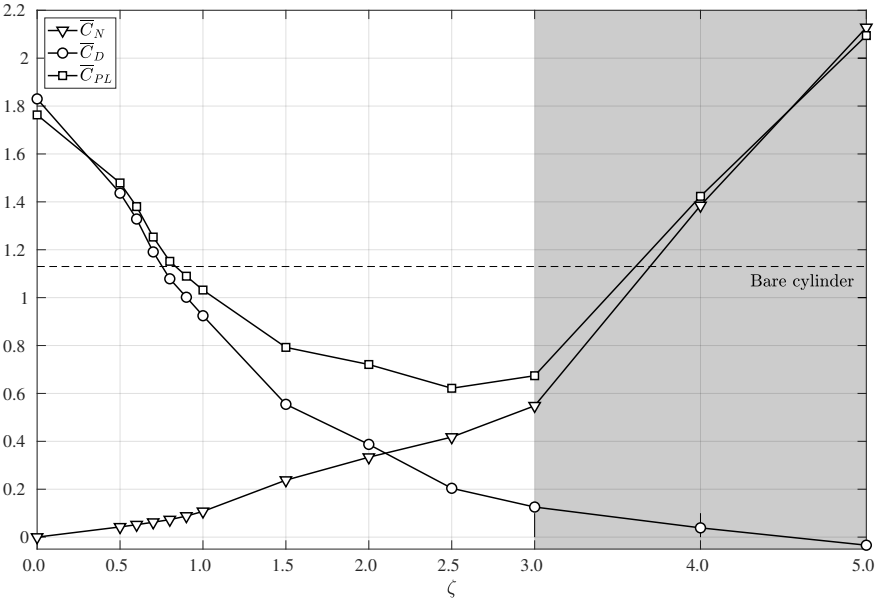

(b) Case 1.

Figure 19: Mean values of the total power-loss coefficient ($\overline{C}_{PL}$) and of its constituents – power-loss due to shear ($\overline{C}_N$) and to drag ($\overline{C}_D$) – for cases 0 and 1. Shading indicates regions of vortex-shedding suppression.

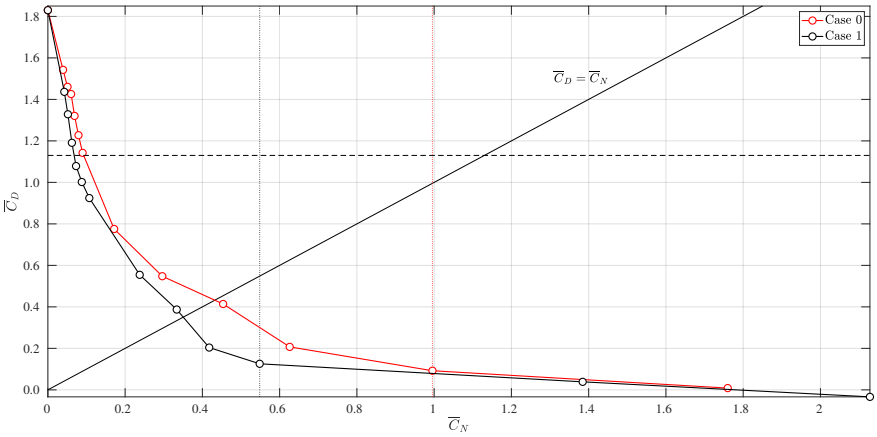

Figure 20: $\overline{C}_D$ vs $\overline{C}_N$. Dotted vertical lines point to the onset of a controlled, steady-wake condition.

the effectiveness of the system (in either configuration, although case 1 was more efficient). Furthermore, the frontier $\overline{C}_D = \overline{C}_N$ divides the figure into drag- and shear-dominated regions. At higher ζ, $\overline{C}_N$ dominated the composition of $\overline{C}_{PL}$ as it can be promptly noted for $\zeta = 5.0$. Unless propulsion is desired, started for $\zeta = 5.0$ in case 1, limiting $\zeta < 5$ as in the scope of this work aptly fulfills the purpose of suppression of vortex shedding with drag reduction.

4. Conclusion

A system comprised of a main cylinder fitted with 8 rotating peripheral rods distanced radially by a gap from the central body was analysed in this paper. DES simulations were conducted in turbulent regime at $Re = 10^3$. Two cases were assessed: case 0, where all rods adopted a uniform absolute speed value $|\omega_n|$; and case 1, where the angular velocities ω_n of the rods were inspired by potential-flow theory, thus weighting the relative position of the rods. The two cases were constrained to the same input kinetic energy. The parameter ζ multiplied the speed of all rods at once to evaluate the effect of the active devices for different rotation rates.

Vortex dynamics showed that the use of the potential-flow-inspired system produced a more effective way to mitigate vortex shedding. In general, mean drag ($\overline{C}_D$) and RMS of the fluctuating lift ($\hat{C}_L$) acting upon the entire system were significantly reduced using the new configuration compared with the uniform setup. This result was associated with a narrower wake and an elongated formation length, leading to increased shedding frequency prior to the transition of the wake to a steady condition.

Besides, it was demonstrated by means of Q-contours of turbulent viscosity that the spinning rods led to a two-dimensional "laminarised" state of the flow, that progressively eliminated turbulent structures. *Vortex dislocations*, in the sense of the vortex-shedding *mode B* of vorticity transfer were detected streamwise, provided the system was supplied with enough actuating power (sufficiently high ζ). One might wonder whether the spinning rods' effect was to "lower the effective Re-regime", taking in consideration that mode B was reported by Williamson (1996) in a wake-transition regime, rather than in a sub-critical regime as in the present work.

Although the loads acting on the group of rods made up by P_n (or, alternatively, by P'_n) seemed insensitive to the distinction between cases 0 and 1, analysis of the individual contributions of the rods showed preference of case 1 to concentrate the effort on the intermediate rods (P_2 and P_3) more intensely than in case 0 for greater ζ, discerning case 1 from case 0 in greater power expenditure. Nevertheless, this behaviour at the upper limit of the velocities hereby analysed was offset by lower $\hat{C}_L$ and $\overline{C}_D$ throughout most ζ-regimes and a more efficient control of the wake. Indeed, because the end rods (P_1 and P_4) were located near stagnation regions, they were expected to interact less with boundary and shear layers. Hence, case 1 anticipated vortex-shedding suppression relative to case 0, thus required lower input kinetic energy and actuating power to control the vortex street.

Concerning the entire system, the present study showed that the power-loss coefficient (that includes power spent to counteract shear and effort to reduce drag) – resulting either from the new configuration or from the uniform-speed one – was able to lower the power-loss coefficient below the value of the mean drag of the reference case of a plain cylinder. Thus, the system proved to behave more efficiently than to employ a bare cylinder, because the reduction in mean drag by the rods was accompanied by such small actuating power that cumulatively $\overline{C}_D + \overline{C}_N$ for the entire system did not equal the mean drag of the bare body. Furthermore, our results present a trend wherein wake suppression accompanied by $(\overline{C}_{PL})_{\text{case 1}} < \overline{C}_{D,\text{Bare}}$ might be achievable even in a steady condition (although more simulations would be required to corroborate with this assertion).

Finally, we were able to show that potential-flow-inspired angular velocities are effective even in turbulent, three-dimensional regime to reduce hydrodynamic loads, and beyond, to suppress vortex shedding entirely. Future work should concern with the system free to respond to vortex-induced vibrations and with multi-objective optimisation of the angular velocities.

References

Carvalho, I., Assi, G., 2022. Enhanced control of the turbulent flow past a circular cylinder with rotating rods inspired by an inviscid solution. Journal of Fluids and Structures 113, 103652.

Carvalho, I.A., Assi, G.R.S., Orselli, R.M., 2021. Wake control of a circular cylinder with rotating rods: Numerical simulations for inviscid and viscous flows. Journal of Fluids and Structures 106, 103385.

Shukla, R.K., Arakeri, J.H., 2013. Minimum power consumption for drag reduction on a circular cylinder by tangential surface motion. Journal of Fluid Mechanics 715, 597–641. doi:10.1017/jfm.2012.537.

Williamson, C.H.K., 1996. Vortex dynamics in the cylinder wake. Annual review of fluid mechanics 28, 477–539.